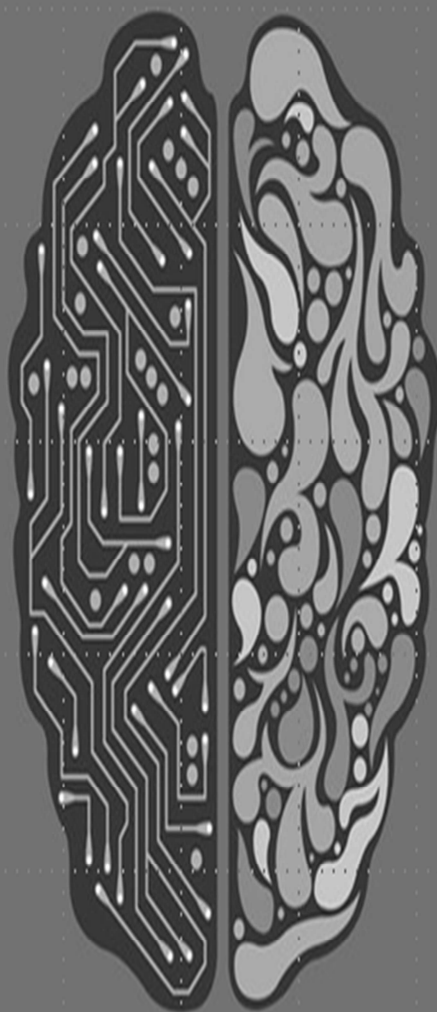


Volume 2 Issue 1 December 2019

ISSN 2635-4608

# Journal of Medical Imaging



# Journal of Medical Imaging

## Editor-in-Chief

Dr. Elias Lee

## Advisory Board

Dr. Maria Claudia Goncalves, State University of Campinas , Brazil

Dr. Alexander E. Berezin, Hospital Universitario de Getafe, Madrid-Spain

Dr. Pablo Alejandro Cardinal Fernandez, Zaporozhye State Medical University, Ukraine

Dr. Shalea Piteau, Nuclear Medicine Unit, S.M. della Misericordia Hospital, Italy

Dr. Anna Margherita Maffione, Queen's University, Kingston

Dr. Wilmer Noe Delgado Luengo, Ovidius University of Constanta, Romania

Dr. Laura Mazilu, Universidad del Zulia, Venezolano

Dr. Claudia Fernanda Dick, King Saud Bin Abdulaziz University for Health Sciences, Saudi Arabia

Dr. Hazem Aqel, Johns Hopkins University, USA

Dr. Siddharth Arun Wayangankar, Medical University, Bulgaria

Dr. Ayman Shehata Mohammed Ahmed Osman El-Shazly, Assiut University, Assiut, Egypt

Dr. Vaibhav Sundriyal, Research Scientist, ODU Research Foundation, Norfolk, VA

Dr. J. E. Jung, Daegu Health Collage, Republic of Korea

Dr. Byungchae Lee, Korea Atomic Energy Research Institute, Republic of Korea

Dr. Yoonjin Oh, Samsung Medical Center, Republic of Korea

Dr. YashPal Singla, LSCP, Sirsa, India

Dr. Aliakbar Kakouei, University of Tehran, Tehran, Iran

# Journal of Medical Imaging

**Content**

ISSN 2635-4608

j. med. Imaging(ScholarGen) Volume 2, Issue 1, December 2019

## **1 MRI based theraputic Vector**

-----*SangBock Lee, V. R. singh*

## **11 MR Weighted Image Discrimination by Artificial Intelligence**

-----*Giljae Lee, Gyehwan Jin, Hwunjae Lee, Jaeun Jung*

## **25 Optimized Feature Parameter Extraction of Brain Tumor MRI**

-----*Jingyu Kim, \*SangBock Lee, Gyehwan Jin, Byungju Ahn, Jooyeon Kim, Sangjin Lim*

# MRI based Therapeutic Vectors

*\*SangBock Lee, V. R. Singh*

Received: 26 August 2019 / Accepted: 5 October 2019 / Published online: 30 December 2019

©The Author(s) 2019

**Abstract-** The development of simultaneous therapy and imaging systems (Theranostics) for micro RNA (miRNA) is demanded the clinical application of RNA interference (RNAi) in cancer treatment and immune therapy. In this paper, we report a pH-sensitive, magnetic nanoparticle-based miRNA delivery system that can enable the safe and effective delivery, imaging by high-resolution Magnetic Resonance Imaging (MRI) and therapeutic ability through regulating of tumor metastasis and immune evasion via miRNA34a. Cationic poly-L-lysine-graft (PL) with a reactive silane moiety was stably immobilized onto the surface of the assembled manganese ferrite nanoparticles (MFs) through an emulsion process, ensuring high water solubility, enhanced MR contrast effect, and endosome-disrupting functionality.

The MRI based theranostic nanovectors (MNVs) were then complexed with miRNA34a via electrostatic interaction to verify the regulation for cancer metastasis by CD44 and immune avoidance by regulating PD-L1. These results showed a novel platform for synergetic cancer therapy based on miRNA.

**Key Word: miRNA34a, CD44, PD-L1, Cancer Treatment, Immune Evasion, MRI, Theranostics**

## I. Introduction

MicroRNAs (miRNAs)—small (20–22 nucleotide), endogenous, non-coding RNAs—act as regulators of gene expression at the post-transcriptional level through RNA interference. Mature miRNAs, which can regulate multiple target genes, associate with 3'-untranslated regions (3'-UTR) of specific target mRNAs to suppress translation and occasionally lead to their degradation. [1][2] Also, microRNAs (miRNAs) are actively involved in a variety of cellular processes, including differentiation, proliferation, and apoptosis. [3] Aberrant miRNA levels have an impact on many diseases, such as cancer, where miRNAs serve as both tumor suppressors and oncogenes. [3] In addition,

S.B. Lee 

*\*SangBock Lee*

*Department of Radiology, Nambu University, 62271, Gwangju, Republic of Korea*

*\*corresponding author*

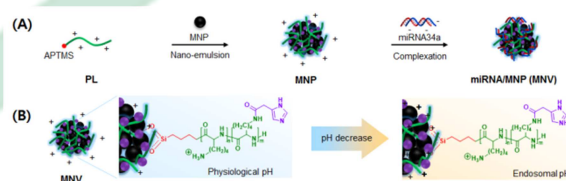
*V. R. Singh*

*Director, PDM University, India*

*e-mail : [vr-singh@ieee.org](mailto:vr-singh@ieee.org)*

Programmed death-ligand 1 (PD-L1) is a 40kDa type 1 transmembrane protein that has been considered to play a major role in suppressing the [immune system](#) during particular events such as pregnancy, tissue [allografts](#), autoimmune disease and other disease states such as hepatitis, it may allow cancers to evade the host immune system. [4][5] An analysis of 196 tumor specimens from patients with [renal cell carcinoma](#) found that high tumor expression of PD-L1 was associated with increased tumor aggressiveness and a 4.5-fold increased risk of death. [6] Consequently, tumor can exploit the PD-L1 pathway to inhibit the anti-tumor immune response. [7] Recently, PD-L1 which plays an important role in the antitumor effect, has been studied in the world, especially, research in the miRNA-mediated regulation of PD-L1 has been widely progressed. [7] It had previously demonstrated that miR-200 inhibited PD-L1, explaining how prevented epithelial-to-mesenchymal transition and metastasis in lung cancer, Welsh et al have investigated the role of miR34a in regulating PD-L1 activity, also, miRNA34a modulates PD-L1 to induce immune evasion, as well as to regulate cancer metastasis by regulating CD44, an important marker of cancer. [8][9] However, it is big issue for delivering miRNA, in order to safely deliver of Gene such as miRNA in vivo, appropriate delivery systems are also required for efficient and safe delivery of miRNAs. Recent research have evaluated many nonviral vectors incorporating imaging agents (i.e., magnetic nanoparticles, gold nanoparticles and fluorescence molecules) as promising carriers for simultaneous imaging and gene delivery. [10][11] These research have shown that such vectors can improve therapeutic efficacy and tumor accumulation through real-time monitoring of the miRNA-delivery process, for the clinical applicability of miRNA-mediated

therapy, simultaneous imaging and gene delivery is important to improve therapeutic efficacy, bio-distribution, and tumor accumulation of nanovectors by facilitating visualization of the miRNA delivery process. For this purpose, a number of inorganic formulations (i.e., magnetic nanoparticles, gold nanoparticles, and quantum dots, etc.) are being evaluated as attractive materials for miRNA delivery and imaging due to their special properties such as facile surface modification, size control, and imaging modalities. Among them, magnetic nanoparticles (MNPs) enable the monitoring of miRNA delivery by non-invasive and real-time magnetic resonance imaging (MRI), because this technique can rapidly acquire multi-informational high resolution images. To accomplish this, miRNAs need to be reversibly packed into MNPs allowing them to be transported into the cytoplasm and carry out the RNAi functional mechanism effectively. Several approaches can be implemented to introduce miRNA into MNPs, including cleavable linkers, electrostatic interactions, or incorporation into polymeric matrix composites. For the safe and effective intracellular delivery of miRNA with MR contrast agents, the nanopatform should 1) be sufficiently cationic to condense miRNA, 2) have no significant inhibition of growth and proliferation on cells, 3) be promptly



**Scheme.** (A) Schematic illustration of the synthesis of pH-sensitive magnetic nanovectors (MNV) with and magnetic nanoparticles (MNPs) through the emulsion process, and the formation of MNV/miRNA34a complexes *via* electrostatic interaction. (B) Schematic illustration of a rapid

change in the surface charge of MNV in response to a reduction in pH as a result of pH-activated protonation.

disassembled under pH reduction to lead endosomal escape, and 4) have ultrasensitive magnetic properties after uptake. Herein, we developed magnetic nanovectors (MNVs) by the emulsion and solvent evaporation method using pH-sensitive polycations that stabilize and envelop MNPs in Schematic image, and demonstrated their utility for cancer detection by MRI and synchronous delivery of therapeutic miRNA. For the complexation of miRNA and to provide a buffering effect under acidic pH, the hydrophilic and cationic homopolymer poly-L-lysine (PL) with a silane terminal group was first prepared by consecutive processes of ring-opening polymerization and deprotection. The obtained PL was used not only for the self-assembly of the manganese ferrite ( $\text{MnFe}_2\text{O}_4$ ) nanoparticles (MFs) but also for gene loading at the outer layer of MFs, finally producing water-dispersible, magnetic particles core-polycation shell nanostructures. These results demonstrate that magnetic nanovectors have potential as theragnostic nanosystems for regulating immune evasion and tumor metastasis based on miRNA in effective cancer therapy.

## II. Materials and Methods

### A. Materials

$\text{N}^6$ -carbobenzyloxy-L-lysine (LysZ), 4-imidazoleacetic acid, (3-aminopropyl) trimethoxysilane (APTMS), 1-ethyl-3-(3-dimethylaminopropyl) carbodiimide (EDC) hydrochloride, trifluoroacetic acid (TFA), hydrobromic acid solution (33 wt % in acetic acid) (HBr/AcOH), anhydrous tetrahydrofuran (THF),

$\text{N,N}$ -dimethylformamide (DMF), dimethylsulfoxide (DMSO), 1N sodium hydroxide (NaOH) solution, iron (III) acetylacetonate, manganese (II) acetylacetonate, 1,2-hexadecanediol, lauric acid, lauryl amine, benzyl ether, deuterium oxide ( $\text{D}_2\text{O}$ ), and dimethylsulfoxide- $\text{d}_6$  (DMSO- $\text{d}_6$ ) were purchased from Sigma-Aldrich (St. Louis, MO, USA). Triphosgene was acquired from Tokyo Chemical Industry Co. (Tokyo, Japan), and 1-hydroxybenzotriazole hydrate (HOBt) was obtained from Daejung Chemicals & Metals Co. (Shiheng, Korea). n-Hexane and diethyl ether were obtained from Ducksan Scientific Co. (Seoul, Korea) The miRNA34a (miR34a) (Sense : ACA ACC AGC UAA GAC ACU GCC A/iSp9//3ThioMC3-D, antisense : UGG CAG UGU CUU AGC UGG UUG U) was purchased from Messenger of Biotechnology Co. (Gyeonggi, Korea), and the hydroxyl PEG Thiol was purchased Nanocs.

### B. Methods

#### 1. Synthesis of $\text{N}^6$ -carbobenzyloxy-L-lysine N-carboxyanhydride (LysZ-NCA)

Synthesis of N-carboxyanhydride of L-lysine was conveyed out by the Fuchs-Farthing method using triphosgene. To make ready  $\text{N}^6$ -carbobenzyloxy-L-lysine (LysZ) N-carboxyanhydride (LysZ-NCA), LysZ (2 g, 7.13 mmol) was suspended in 145 mL of anhydrous THF. Triphosgene (0.85 g, 2.85 mmol) solution dissolved in 5 mL of THF was injected into the LysZ-suspended solution using a syringe under nitrogen atmosphere. The reaction was performed at  $35^\circ\text{C}$  for 3 hr under magnetic stirring, and the appearance of the reactant solution changed from cloudy to clear after all LysZ molecules were transformed into LysZ-NCA. The solvent was filtered through a  $0.2\text{-}\mu\text{m}$  PTFE syringe filter

(Advantec MFS, Inc., Japan) to remove impurities, followed by evaporation of the filtrate under the reduced pressure. The concentrated reactants were introduced to cold excess n-hexane, and the n-hexane/THF mixture was then recrystallized at -20°C overnight. The precipitants were purified three times by filtration and dried at room temperature *in vacuo*. Yield: 70%. FT-IR (cm<sup>-1</sup>):  $\nu = 3340$  (s, NH), 3070-2870 (s, CH<sub>2</sub>), 1855/1810/1774 (s, C=O in anhydrides of NCA), 1745 (s, C=O in Z group), 1685 (s, C=O in amide of NCA) 1528 (s, NH in amide of NCA). <sup>1</sup>H-NMR (400 MHz, DMSO-d<sub>6</sub>, ppm):  $\delta = 9.09$  (w,  $\alpha$ -NH), 7.54-7.26 (s, Ar-H in benzyl groups), 5.04-5.00 (s, -CH<sub>2</sub> in benzyl groups), 4.44-4.41 (w,  $\alpha$ -CH), 3.01-2.96 (m,  $\epsilon$ -CH<sub>2</sub>), 1.72-1.30 (m,  $\gamma$ -CH<sub>2</sub> and  $\delta$ -CH<sub>2</sub>).

## 2. Synthesis of APTMS-initiated poly-L-lysine (PL) by ring opening polymerization

To synthesize poly (N<sup>6</sup>-carbobenzyloxy-L-lysine) (PLZ), the polymerization of LysZ-NCA initiated by APTMS proceeded as follows. Briefly, LysZ-NCA (10 g, 32.65 mmol) was dissolved in 50 mL of anhydrous DMF. APTMS (73.16 mg, 0.41 mmol) was injected into the solution as an initiator using a syringe under a blanket of nitrogen, and the mixture was reacted at 40°C for 24 hr. The solvent was evaporated under reduced pressure and precipitated in excess cold diethyl ether. The purified precipitates were isolated by repeated filtration and dried under high vacuum. Yield: 61.11%. FT-IR (cm<sup>-1</sup>):  $\nu = 3198$  (s, NH), 3062-2866 (s, CH<sub>2</sub>), 1693 (s, C=O in Z group), 1653 (s, C=O in amide), 1530 (s, NH in amide). <sup>1</sup>H-NMR (400 MHz, DMSO-d<sub>6</sub>, ppm):  $\delta = 8.44$ -7.88 (w,  $\alpha$ -NH), 7.53-7.19 (s, Ar-H in benzyl groups), 4.99 (s, -CH<sub>2</sub> in benzyl groups), 4.31-4.11 (w,  $\alpha$ -CH), 2.95 (m,  $\epsilon$ -CH<sub>2</sub>), 1.62-1.27 (m,  $\gamma$ -CH<sub>2</sub> and  $\delta$ -CH<sub>2</sub>). The obtained PLZ was further

characterized by gel permeation chromatography (YL9100 HPLC, Young Lin Instrument Co., Ltd., Korea) equipped with two Waters styragel HR3 columns (Waters Co., Milford, MA) and a refractive index detector through HPLC-grade DMF at 1.0 mL/min. The molecular weight distribution ( $M_w/M_n$ ) of the polymer was determined to be 1.2. To remove the Z protection groups, PLZ (7 g, 0.33 mmol) was dissolved in 70 mL of TFA and then 10 mL of HBr/AcOH was added to the mixture. The mixture was gently stirred at room temperature for 1.5 hr and the resulting product was isolated three times by filtration with excess diethyl ether. The polymer was further dialyzed against multiple ultrapure distilled water.

## 3. Fabrication of PL-coated magnetic nanoparticles

Magnetic Nanovectors (MNVs) as gene loadable MR imaging agents were prepared by the nano-emulsion method. Firstly, monodisperse manganese ferrite (MnFe<sub>2</sub>O<sub>4</sub>) nanoparticles (MFs) were synthesized by the thermal decomposition of metal-organic precursors in the presence of nonpolar organic solvents. In detail, iron (III) acetylacetonate (2 mmol), manganese (II) acetylacetonate (1 mmol), 1,2-hexadecanediol (10 mmol), lauric acid (6 mmol), and laurylamine (6 mmol) were dissolved in 20 mL of benzyl ether. The solution was preheated to 200°C for 2 hr under an ambient nitrogen atmosphere and refluxed at 300°C for 1 hr. After cooling the reactants to room temperature, the products were purified using an excess of pure ethanol. Approximately 11-nm MFs were synthesized using the seed-mediated growth method. Twenty milligrams of the as-synthesized MFs were dissolved in 4 mL of n-hexane and subsequently added into 20 mL of DW containing 50, 100, or 200 mg of PL. After mutual

saturation of the organic and aqueous phases, the mixture was ultrasonicated at 200 W for 20 min with vigorous stirring at 1,500 rpm, and stirred for 4 hr to evaporate the residual hexane.

#### 4. Preparation of miRNA loaded magnetic nanoparticles

The miRNA condensation ability of MNPs was confirmed by the gel retardation assay. To compare miRNA-loading ability, miRNA was also complexed with varying amounts of MNPs. The prepared complexes were mixed with 6x HiQ™ goRed (Genepole, Seoul, Korea), then loaded into a 2% agarose gel (w/v), and electrophoresed in Tris – borate – EDTA (TBE) buffer at 100 V for 20 min. The retardation of complexes was visualized by a UV lamp using a Gel Doc System.

### III. Experiments.

#### 1. Characterizations of magnetic nanovectors

The average hydrodynamic diameters and zeta potentials of the obtained magnetic Nanovectors (MNVs) were measured using dynamic laser scattering at room temperature. Their size distributions and morphologies were observed by transmission electron microscopy at an accelerating voltage of 200 kV. The concentration of Mn plus Fe ions in the MNVs was measured by using inductively coupled plasma-atomic emission spectrometry (ICP-AES) analysis. The magnetic hysteresis loop and the saturated magnetization value were obtained using a vibrating sample magnetometer at 25°C. The amount of MFs encapsulated in MNVs was measured by thermal gravimetric analysis. The T2 relaxivity ( $r_2$ ) data of the MNV solution were obtained through

magnetic resonance (MR) imaging analysis.

#### 2. Cell viability test

The cytotoxicity of MNVs in gastric cancer MDA-MB-231 cells was evaluated by a colorimetric assay, based on the cellular reduction of 3-(4,5-dimethylthiazoly-2)-2,5-diphenyltetrazolium bromide (MTT) (Cell Proliferation Kit I, Roche, Germany) in metabolically active cells. MDA-MB-231 cells ( $1 \times 10^4$  cells/well) were seeded into 96-microwell plates, incubated in RPMI 1640 medium containing 5% fetal bovine serum (FBS) and 1% antibiotics at 37°C overnight in a humidified atmosphere with 5% CO<sub>2</sub>, and then treated with MNVs containing medium with 5% FBS at various concentrations for additional 24 hr. After incubation, the yellow MTT solution was added and the formazan crystals formed were solubilized with 10% sodium dodecyl sulfate in 0.01 M HCl. Then the relative percentage of cell viability was calculated from the formazan intensity ratio of treated to non-treated control cells and shown as an average  $\pm$  standard deviation.

#### 3. MR imaging procedures

We performed solution and in vitro, in vivo MR imaging experiments with a 4.7 T clinical MRI instrument. The R2 values (T2 relaxation rate,  $1/T_2$ ,  $s^{-1}$ ) of the MNV solution and miR34a-MNP treated cells ( $1 \times 10^7$ ) were measured by using the conventional T2 sequence at room temperature. For the acquisition of T2 weight MR images of MNV solution, MNV treated cells and in vivo MR imaging the following parameters were adopted: resolution of xxx x xxx mm, section thickness of x mm TE = x ms, TR = x ms, and number of acquisitions = 1, The  $r_2$  ( $Mm^{-1}s^{-1}$ ) is equal to the ration of the R2 to the MNV concentration.

#### 4. Cellular uptake of MNVs

To prepare cellular TEM samples, MDA-MB-231 cells ( $1 \times 10^6$ ) were harvested after TrypLE™ (Gibco®) treatment, washed in triplicate with blocking buffer (0.03% bovine serum albumin and 0.01%  $\text{NaN}_3$  in phosphate-buffered solution, pH 7.4 and 10 mM) to prevent non-specific binding, and gently pelleted. Subsequently, the cells were suspended in MNV solution (0.46  $\mu\text{g}/\text{mL}$ ) and incubated for 30 min on ice and 30 min at 37°C. After incubation, the cells were washed three times with blocking buffer and fixed according to the standard fixation and embedding protocol for resin-section TEM. The sample resin blocks were trimmed and sectioned using a LEICA Ultracut UCT Ultramicrotome (Leica Microsystems Ltd., Austria). Cellular uptake of MNVs was also examined by the Prussian blue staining method. To stain magnetic components in MDA-MB-231 cells treated with MNVs (0.46  $\mu\text{g}/\text{mL}$ ), the cells were incubated with 2% potassium ferrocyanide in 10% HCl and then counterstained with Nuclear Fast Red (Sigma-Aldrich). Cellular internalization of the MNVs was observed by TEM at an accelerating voltage of 80 kV and an epi-fluorescence microscope.

### IV. Result & discussion

#### 1. In vitro transfection and quantitative reverse transcriptase-polymerase chain reaction (qRT-PCR) analysis

To measure CD44, PDL1 mRNA expression levels in cancer cells, real time qRT-PCR analysis with internal standards was performed. Firstly, MDA-MB-231 cells ( $2 \times 10^5$  cells/well) were seeded in six-well plates containing 2 mL culture medium supplemented with 5 % FBS and incubated at 37°C overnight to reach 70% confluence at the time of

transfection. The culture medium was then replaced with serum-free medium and 100  $\mu\text{L}$  of MNPs containing miR34a or control miR34a (100 pmol) at a polycation/miRNA weight ratio of 1:2 was added to each well. As a control, MDA-MB-231 cells were also transfected with free miR34a or control miR34a. After 6 hr incubation, the medium was replaced with 2 mL fresh culture medium and further incubated at 37°C for 48 hr. The cells were harvested 48 hr after transfection, and total RNA was isolated from the cells with the RNeasy® Plus Mini Kit (QIAGEN, Hilden, Germany), according to the manufacturer's instructions. Complementary DNA (cDNA) was synthesized from 2  $\mu\text{g}$  of total RNA using the High Capacity RNA-to-cDNA kit (Applied Biosystems®). The resulting cDNA was amplified by PCR, conducted with the QuantiMix SYBR Kit (PhileKorea Technology, Daejeon, Korea) on a real-time PCR system (LightCycler® 480 System, Roche). Primer sequences were as follows: CD44, forward 5'-CCTCTT GGCCTTGGCTTTG-3' and reverse 5'-TCCATTGCCACTGTTGATCA-3'; PD-L1, forward 5'-AAATGGAACCTGGCGAAAGC-3' and reverse 5'-GATGAGCCCCTCAGGCATTT; GAPDH, forward 5'-GCTCTCTGCTCCTCCTGTTC-3' and reverse 5'-TGACTC CGACCTTCACCTTC-3'. The PCR conditions were as follow: initial denaturation at 95°C for 10 min; 45 cycles of amplification at 95°C for 10 sec, at 60°C for 10 sec, and at 72°C for 10 sec. Each sample was performed in triplicate. The relative CD44 mRNA expression value was normalized to the endogenous reference gene (GAPDH) in the corresponding samples and relative to non-treated cells, and calculated by the  $\Delta\Delta C_t$  method.

#### 2. In vitro Western blot analysis

To assess the down-regulation of the CD44, PD-

L1 gene in MDA-MB-231 cells, the cells were harvested and lysed in cold RIPA buffer (Pierce<sup>®</sup>, Thermo Scientific) containing a protease inhibitor cocktail tablet (complete Mini, Roche). The lysates were incubated at 4°C for 30 min and centrifuged at 13,000 rpm for 15 min. The supernatants were analysed for protein concentrations using the bicinchoninic acid (BCA) Protein Assay (Pierce<sup>®</sup>). Equal amounts (20 µg) of protein were subjected to electrophoresis on sodium dodecyl sulfate (SDS)-polyacrylamide gels and then transferred to a nitrocellulose blotting membrane (Amersham™ Hybond ECL, GE Healthcare). The blotted membranes were immunostained with antibodies specific for CD44 (156-3C11, Cell Signalling Technology, Inc., USA), PD-L1 (22C3, Dako, Inc, USA) and GAPDH antigens (6C5, Santa Cruz Biotechnology, Inc., USA). The signals were developed by a standard enhanced chemiluminescence (ECL) method (Pierce<sup>®</sup> ECL Plus Western Blotting Substrate) according to the manufacture's protocol.

### 3. Wound healing assay

For the evaluation of the migration and mobility of MDA-MB-231 cells treated with MNVs, the wound healing assay was carried out. The cells were transfected with nanovector formulations with miR-34a or control miR and grown to 100% confluence in culture media. Using a sterile pipette tip, the cell monolayer was mechanically scratched inducing the wound and further incubated with culture media for 4 days. The

images of the wound closing were captured with an inverted microscope.

### 4. Invasion assay analysis

At first, to lay HUVEC cells, Coat the inside of transwell with 50µL Fibronectin (10 µg/mL) at the bottom and dry for 2-3 hours at RT. Coat the bottom of transwell with 10µL of 0.2% gelatin and dry for 30 min at RT. After that add  $2 \times 10^4$  endothelial cells (HUVEC) in 50µL of culture medium (M199) to insert. And culture the cells for 48 hours until forming monolayer. At seconds, in order to stain the cells, when the cells reached 70% confluence remove the medium from the dish. And add fresh medium (0% FBS) with Cell tracker dye (0.5µM) Incubate the cells for 1hours. Replace the dye working solution with culture medium (10% FBS) for 30min. To lay tumor cells which treated cell tracker, harvest tumor cells with 0% culture medium, and add  $1 \times 10^5/50 \mu\text{L}$  tumor cells to insert. And add 605 µL with culture medium (10% FBS) to the lower chamber. Incubate the cells for 48 hours. To measure cell which passing the MEM, remove the upper cells of membrane by cotton swab. Lysis the cells on lower membrane with 200 µL lysis buffer, 2-3 hours at RT. Read absorbance (Abs/Em : 492/517)

### 5. In vivo tumor growth inhibition, target gene silencing and immune evasion

For the inhibition study of tumor growth using MNVs, here we used a subcutaneous xenograft

tumor model that allows routine and facile measurements of tumor volume. A cancer model was established by subcutaneously injecting MDA-MB-231 cells ( $10^7$  cells suspended in 50 mL of PBS per animal) into the breast of the BALB/c-nude mice. Tumor bearing mice were randomized into 3 different groups for treatments (non-treated, control miRNA34a/MNV treated groups and miR-34a/MNV-treated groups), when the tumor volume increased to  $200 \text{ mm}^3$ . Prior to administration of each formulation, animals were anesthetized and injected with control miRNA34a/MNV and miR-34a/MNV (1 nmole of miR-34a per injection) through the tail vein twice per week for 3 weeks. The tumor volume was calculated using the formula:  $V = \frac{4}{3} \pi \left(\frac{a}{2}\right) \left(\frac{b}{2}\right)^2$ , where a and b are the half length of the minor and minor axis of tumors determined by a caliper. All mice were sacrificed after 7 weeks post-treatment and the extracted tumor tissues were used for H&E staining, TUNEL assay. The tumor sections were then counterstained with Hoechst 33342 and PE mouse anti-human CD44 (BD Pharmingen, Cat. No. 550989), PD-L1 (Dako, Cat. No. 22C3). The expression levels of CD44, PD-L1 in the excised tumor tissues after crushing in liquid nitrogen were also verified by western blot assay using the same procedures as described in in vitro analysis

## V. Conclusion

We present the pH-sensitive, magnetic nanoparticle-based miRNA delivery system that can facilitate the safe and efficient delivery,

imaging by high resolution MRI and therapeutic ability through regulating of tumor metastasis and immune evasion via miRNA34a. Cationic poly-L-lysine-*graft* (PL) with a reactive silane moiety was stably immobilized onto the surface of the assembled manganese ferrite nanoparticles (MFs) through an emulsion process, ensuring high water solubility, enhanced MR contrast effect, and endosome-disrupting functionality. We verified the in vivo and in vitro specific CD44 gene knockdown effects of MNVs in MDA-MB-231 cells using both qPCR and Western blot analysis. We found that the regulation through miR34a enable to cancer metastasis by CD44 and immune avoidance by regulating PD-L1. Consequently, we designed theranostic system would be beneficial to expand research on miRNA based and immune therapy for cancer.

## Competing interests

The authors declare that there is no conflict of interest regarding the publication of this paper.

## Acknowledgments

This study was supported by Nambu University research fund of 2017.

## [References]

1. Minju Ha, V. Narry Kim, "*Regulation of microRNA*", Nature Reviews Molecular Cell Biology 2014, **15**:509-524.
2. Lin He, Gregory J Hannon, "*MicroRNAs: small RNAs with a big role in gene regulation*", Nature Review Genetics 2004, **5**:631.

3. George A. Calin, Carlo M. Croce, "**MicroRNA signatures in human cancers**", Nature Review Genetics 2006, **6**: 857-866
4. Keisuke Kataoka<sup>1</sup>, Yuichi Shiraishi, et al, "**Aberrant PD-L1 expression through 3'-UTR disruption in multiple cancers**", Nature 2016, **534** : 402-406
5. Diana Romero, "**Benefit with anti-PD-L1**", Nature Reviews Clinical Oncology 2017, **14** : 70-71
6. Thompson RH, Gillett MD, Cheville JC, Lohse CM, et al, "**Costimulatory B7-H1 in renal cell carcinoma patients: Indicator of tumor aggressiveness and potential therapeutic target**", Proceedings of the National Academy of Sciences of the United States of America 2004, **101** : 17174-9
7. Jiabei He, Ying Hu, Mingming Hu, Baolan Li, "**Development of PD-1/PD-L1 Pathway in Tumor Immune Microenvironment and Treatment for Non-Small Cell Lung Cancer**", Scientific Reports 2015, **5** : 13110
8. Maria Angelica Cortez, Cristina Ivan, David Valdecanas, et al, "**PDL1 Regulation by p53 via miR-34**", Journal of National Cancer Institute 2016, **108** : 303
9. Can Liu<sup>1</sup>, Kevin Kelnar, Bigang Liu, Xin Chen<sup>1</sup>, et al, "**The microRNA miR-34a inhibits prostate cancer stem cells and metastasis by directly repressing CD44**", Nature medicine 2011, **17** : 211-215
10. Jae-Hyun Lee, Kyuri Lee, Seung Ho Moon, Yuhan Lee, Tae Gwan Park, and Jinwoo Cheon, "**All-in-One Target-Cell-Specific Magnetic Nanoparticles for Simultaneous Molecular Imaging and siRNA Delivery**", Angewandte Chemie International Edition 2009, **48** : 4174-4179
11. Huan Meng, Monty Liong, Tian Xia, Zongxi Li, et al, "**Engineered Design of Mesoporous Silica Nanoparticles to Deliver Doxorubicin and Pgp siRNA to overcome Drug Resistance in a Cancer Cell Line**", ACS Nano 2010, **24** : 4539-4550

# MR Weighted Image Discrimination by Artificial Intelligence

Giljae Lee, Gyehwan Jin, Hwunjae Lee, Jaeun Jung

Received: 7 September 2019 / Accepted: 12 December 2019 / Published online: 30 December 2019

©The Author(s) 2019

**Abstract-** In this study, we proposed a method of learning neural networks by optimizing neural network input parameters to discern MRI-weighted images. To this end, we segmented the weighting domain of MRI. In feature extraction, the original image and segmented image were extracted by DWT, respectively.

A neural network was trained by inputting extracted feature values. As a result of the experiment, it was found that the R-value of the segmented image is closer to 1 than the original image. The reason is that the images obtained by segmenting the areas of the weighted parts already have similarities. Also, it was found that the similarity between T1 and T2 weighted images is high in the same combination, and the similarity is relatively low in different weighted images. The most important issue in medical imaging is ensuring the confidence of radiologists using artificial intelligence. To solve this problem, it is of utmost importance that the algorithm developer and radiological technologist work together to provide a solution that is integrated with the radiologist's workflow.

*Giljae Lee*

*The Korea Health Industry Development Institute*

*e-mail : [korotkoff@khidi.or.kr](mailto:korotkoff@khidi.or.kr)*

*Gyehwan Jin* (✉) **corresponding author**

*Dept. of Radiology, Nambu University*

*e-mail : [ghjin@nambu.ac.kr](mailto:ghjin@nambu.ac.kr)*

*Hwunjae Lee* (✉) **corresponding author**

*YUHS-KRIBB Medical Convergence Research Institute*

*Dept. of Radiology, College of Medicine Yonsei University*

*e-mail : [hjlee7@yuhs.ac.kr](mailto:hjlee7@yuhs.ac.kr)*

*Jaeun Jung*

*Dept. of Radiological science, Daegu Health College*

*e-mail : [ejung@dhc.ac.kr](mailto:ejung@dhc.ac.kr)*

**Key word:** Image processing, Discrete Wavelet Transform, MR pulse sequence, T2 Weighted Image, MR Molecular Imaging, Magnetic nanoparticles

## I. Introduction

Wilhelm Conrad Röntgen discovered a short-wavelength electromagnetic wave called X-rays on November 8, 1895,<sup>[1]</sup> and he won the 1901 Nobel Prize for Physics. For the first time in history, the discovery of X-rays provided the first advance in modern medicine by providing a

way to look inside the human body.

Recent medical images include Digital Radiography (DR), Computed Radiography (CR), Computed Tomography (CT), Positron Emission Tomography (PET), Single Positron Emission Tomography (SPECT), Ultra Sonography, and Magnetic Resonance Imaging (MRI).<sup>[2]</sup>

The World Economic Forum (WEF), chaired by Klaus Schwab, advocated the fourth industrial revolution in 2016[3]. The Fourth Industrial Revolution can be explained by a variety of new technologies that integrate the physical, biological and digital worlds based on big data and affect all sectors, including the economy, industry and healthcare.<sup>[3]</sup> The most impact of the 4th industry on medical care is the issue of big data-based artificial intelligence technology.

In this study, we propose a method of learning neural networks by optimizing neural network input parameters to discern MRI-weighted images. To this end, we segmented the weighting domain of MRI. In feature extraction, the original image and segmented image were extracted by DWT, respectively. A neural network was trained by inputting extracted feature values. If the feature extraction value is input and learned, the inference time of the AI will be reduced and the inference result will be accurate.

## I. Materials and methods

### 1. Magnetic Resonance Imaging

Magnetic resonance imaging forms images by measuring patterns of hydrogen nuclei interacting with magnetic fields in magnetic fields and absorbing and emitting electromagnetic waves at

specific frequencies.<sup>[4]</sup> About 70% of the human weight is body fluid, most of which is water. The proton, the nucleus of the hydrogen atom of water, has a spin in an arbitrary direction, and when it enters a strong magnetic field, the spin direction of the hydrogen nucleus is aligned along the direction of the magnetic field. In this state, when a high-frequency electromagnetic pulse is applied in a vertical direction, the hydrogen nucleus absorbs the energy of electromagnetic waves and changes the spin in the opposite direction of the magnetic field.<sup>[4]</sup> After that, when the pulse is broken, the hydrogen nucleus with reverse spin returns to its original state, releasing weak electromagnetic waves.<sup>[4]</sup> This electromagnetic wave can be detected to track and image the position of the hydrogen atom nucleus from which the electromagnetic wave is emitted. The relaxation time at which the hydrogen nucleus with reverse spin returns to its original state has two values, 'T1' and 'T2', depending on the relaxation coefficient of the spin. The relaxation of the spin of the hydrogen nucleus by interaction with the spin of the surrounding hydrogen nucleus is called spin-spin relaxation, and the time constant thereof is called T2.<sup>[4]</sup> In contrast, the relaxation of spin by interaction with the lattice structure of the surrounding tissue is called spin-lattice relaxation, and this time constant is called T1. T1 and T2 differ greatly depending on the surrounding tissues of the hydrogen nucleus, and the magnetic resonance image makes this relaxation time planar image<sup>[4]</sup>. Figure 1 shows a model of the MRI scanner and Figure 2 shows the images acquired by the MRI scanner. MRI images used in the experiment were obtained from The Cancer Imaging Archive. The obtained image was adjusted to 256 X 256 pixels, and the shape of the

image was transformed into a bit map (\*.bmp) form.

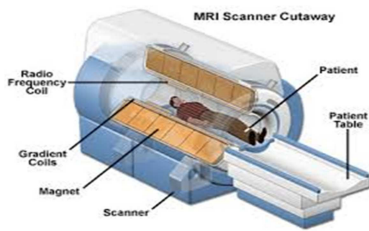


Figure 1. MRI

Scanner[<https://www.javatpoint.com/mri-full-form>]

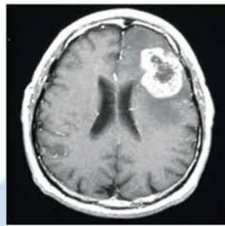


Figure 2. Brain Image

## 2. Image segmentation

In digital image processing, image segmentation is the process of dividing a digital image into segments. The goal of segmentation is to simplify or change the representation of the image to something more meaningful and easier to analyze.<sup>[5][6]</sup> Image segmentation is commonly used to find objects and boundaries (lines, curves, etc.) in an image. More precisely, image segmentation is the process of assigning a label to every pixel in an image so that pixels with the same label share specific characteristics. The result of the image segmentation is a set of segments that collectively covered with a set of contours extracted from the whole image or the image.<sup>[5][6]</sup> Each pixel in the area is similar in terms of some characteristics or calculated properties, such as color, intensity, or texture. Adjacent region varies considerably concerning

for to the same characteristics.<sup>[7]</sup> When applied to image stacks, usually in medical imaging, contours created after image segmentation can be used to create 3D reconstructions using an interpolation algorithm such as the Marching cube.<sup>[8]</sup> Machine vision is a technology and method commonly used in the industry to provide imaging-based automated inspection and analysis for applications such as automated inspection, process control, and robot guidance.<sup>[9]</sup> Machine vision refers to many technologies, software and hardware products, integrated systems, operations, methods, and expertise. Machine vision in the field of systems engineering can be considered distinct from computer vision, a form of computer science.<sup>[9]</sup> We want to solve real problems by integrating and applying existing technologies in new ways. This term is widely used for these functions in industrial automation environments, but it is also used for these functions in other environments such as security and vehicle guidance. The whole machine vision process involves planning the requirements and details of the project and then creating a solution. During run time, the process starts with imaging and then automatically analyzes the image and extracts the necessary information.<sup>[10]</sup> The simplest method of image segmentation is called the threshold method. This method converts grayscale images to binary images based on the clip level. The key to this method is to choose a threshold. Several popular methods are used in the industry, including the maximum entropy method, the balance histogram threshold, the Oats method (maximum variance), and the k-mean clustering.<sup>[11]</sup> Recently, a method for

thresholding computed tomography (CT) images has been developed. The key idea is that, unlike Otsu's method, the threshold is derived from the radiograph instead of the (reconstructed) image.<sup>[12][13]</sup> The new method suggested the use of multidimensional fuzzy rule-based nonlinear thresholds. In these works, the determination of the membership of each pixel for a segment is based on multidimensional rules derived from fuzzy logic and evolutionary algorithms based on the image lighting environment and application.<sup>[14]</sup>

### 3. Discrete Wavelet Transform(DWT)

Wavelet transform was proposed in the mid-1980s, and it has been used in various fields such as signal processing, image processing, computer vision, image compression, biochemistry medicine, etc.<sup>[15]</sup> For image processing, it provides an extremely flexible multi-resolution image and can decompose an original image into different subband images including low- and high-frequencies. Therefore people can choose the specific resolution data or subband images upon their demands.<sup>[16]</sup> A 2-D DWT of an image is illustrated in Figure 3(a). When the original image is decomposed into four-subband images, it has to deal with row and column directions separately. First, the high-pass filter  $G$  and the low-pass filter  $H$  are exploited for each row data, and then are down-sampled by 2 to get high- and low-frequency components of the row. Next, the high- and the low-pass filters are applied again for each high- and low-frequency components of the column, and then are down-sampled by 2. By way of the above processing, the four-subband images are generated:  $HH$ ,  $HL$ ,  $LH$ , and  $LL$ . Each subband

image has its feature, such as the low-frequency information is preserved in the  $LL$ -band and the high-frequency information is almost preserved in the  $HH$ -,  $HL$ -, and  $LH$ -bands. The  $LL$ -subband image can be further decomposed in the same way for the second level subband image.<sup>[17]</sup> By using 2-D DWT, an image can be decomposed into any level of subband images, as shown in Figure 3(b).

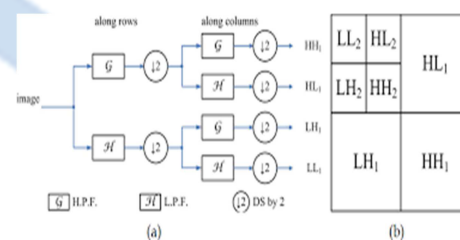


Figure 3. Diagrams of DWT image decomposition: (a) the 1-L 2-D analysis DWT image decomposition process, (b) the 2-L 2-D analysis DWT subband.

### 4. Artificial Intelligence in Medicine

Artificial intelligence (AI) has led to many medical advancements, from AI-based software for the management of medical records to diagnosing and recognizing conditions. Most of the new work on artificial intelligence in the medical field is related to diagnostic technology, and AI systems are trained to recognize the characteristics of various conditions.<sup>[18][19]</sup> Through 'machine learning' (ML), AI provides techniques that uncover complex associations that cannot easily be reduced to an equation.<sup>[20]</sup> For example, neural networks represent data through vast numbers of interconnected neurons in a similar fashion to the human brain. This allows ML systems to approach complex problem solving just as a clinician might by carefully weighing evidence to reach reasoned conclusions.<sup>[21]</sup> However, unlike a single

clinician, these systems can simultaneously observe and rapidly process an almost limitless number of inputs. Furthermore, these systems can learn from each incremental case and can be exposed, within minutes, to more cases than a clinician could see in many lifetimes. Artificial intelligence complements the vast number of digital images created in hospitals, the products of next-generation imaging scanners, especially hybrids that include MRI, CT, PET, and SPECT. In recent years, machine learning algorithms are rapidly being used in medical image analysis. These machine learning techniques are used to extract compact information to improve the performance of medical image analysis. Recently, deep learning methods using deep convolutional neural networks have been applied to medical image analysis to provide promising results.<sup>[22]</sup> The neural network model is shown in Figure 4 below.

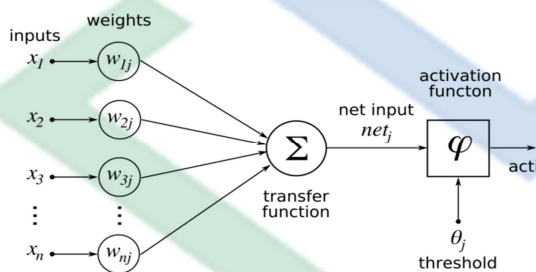


Figure 4. A neural network model.

Applications cover the full spectrum of medical image analysis, including detection, segmentation, classification, and computer-assisted diagnostics.<sup>[23]</sup> As a result, if artificial intelligence and healthcare professionals interact to accommodate deep thinking platforms, such as automation, in diagnosing a patient's disease state, artificial intelligence will play an important role in the analysis of medical image

data, which will only be feasible.<sup>[24][25]</sup>

## II. Experiment and result

For the experiment, we acquired T1 and T2 weighted images from The Cancer Imaging Archive site. The image was preprocessed to 256 x 256 pixels for segmentation and stored in a bitmap format. The stored images were segmented with 127 as the threshold. Six parameters per image were extracted from the segmented image using DWT. We learned neural networks by inputting extracted parameters into the neural networks. Figure 5 is a flow chart showing the whole process of the experiment.

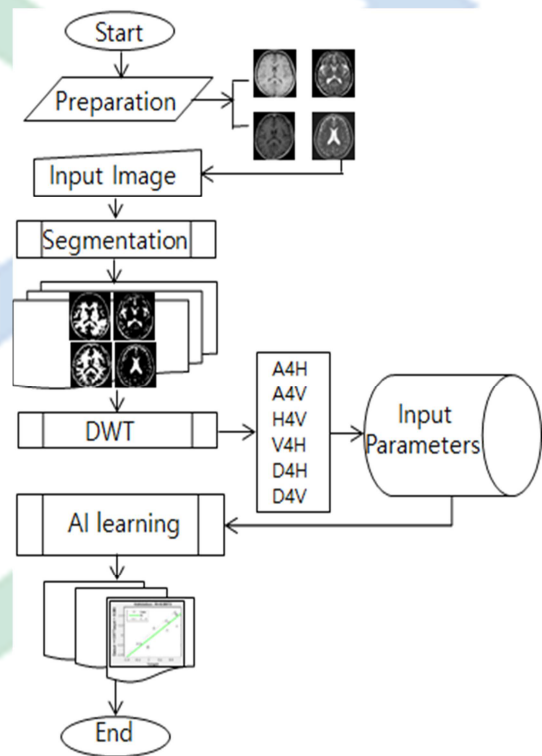


Figure 5 Flow-chart of experiment.

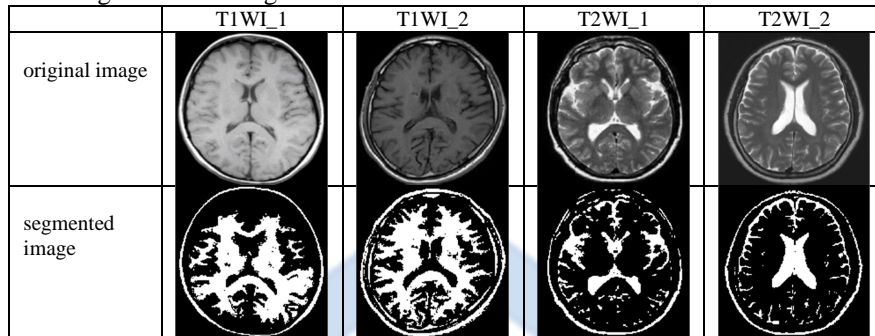
### 1. Image segmentation

Image segmentation plays an important role in many medical imaging applications by automating or

facilitating the depiction of anatomical structures and other areas of interest. We segmented the highlighted portion of the T1 weighted and T2 weighted images

of the MRI image with a threshold of 127. Table 1 below shows the original and segmented images of the T1 and T2 weighted images.

Table 1. Segmentation images



## 2. Discrete Wavelet Transform

In numerical and functional analysis, the discrete wavelet transform (DWT) is any wavelet transform in which the wavelet is sampled discretely. As with other wavelet transforms, the main advantage over Fourier transforms is time resolution. We did MatLab programming to extract six feature parameters. The variable names of the extracted parameters are as follows:

- A4H: Horizontal low frequency
- A4V: Vertical Low Frequency
- H4V: horizontal high frequency
- V4H: vertical high frequency
- D4H: horizontal diagonal high frequency
- D4V: vertical diagonal high frequency

Tables 2 to 9 show extracted feature values by DWT from images of table 1.

Table 2. Feature extraction value of T1WI\_1 original image

A4H	-0.50	-0.49	-0.43	-0.21	-0.23	-0.12	0.07	0.15	0.26	0.31	0.39	0.44	0.49	0.50	0.49	0.42
A4V	-0.50	-0.47	-0.23	-0.31	-0.21	-0.07	0.05	0.14	0.19	0.28	0.37	0.38	0.37	0.43	0.48	0.50
H4V	-0.50	-0.47	-0.39	-0.25	-0.04	0.01	0.18	-0.01	-0.17	0.11	-0.23	0.15	0.17	-0.16	0.27	0.50
V4H	-0.50	-0.49	-0.43	-0.30	-0.20	-0.11	0.08	0.37	0.49	0.37	-0.08	0.35	0.19	-0.21	0.31	0.50
D4H	-0.50	-0.45	-0.22	0.06	0.50	0.27	0.06	-0.03	-0.25	-0.08	-0.12	-0.27	-0.38	-0.32	-0.24	-0.21
D4V	-0.50	-0.02	0.50	-0.06	0.00	0.02	0.09	0.22	0.49	0.19	-0.02	0.01	-0.12	-0.12	-0.15	-0.24

Table 3. Feature extraction value of T1WI\_1 segmental image

A4H	-0.50	-0.49	-0.44	-0.29	-0.38	-0.38	-0.33	-0.23	-0.06	-0.14	0.03	0.43	0.50	0.47	0.14	-0.18
A4V	-0.50	-0.47	-0.26	-0.38	-0.42	-0.43	-0.44	-0.37	-0.02	0.22	0.50	0.36	-0.02	0.28	0.48	0.47
H4V	-0.50	-0.48	-0.42	-0.40	-0.35	-0.35	-0.29	-0.17	-0.07	0.06	-0.14	0.03	-0.07	-0.19	0.50	0.12
V4H	-0.50	-0.49	-0.47	-0.41	-0.38	-0.37	-0.08	0.10	0.50	0.15	0.08	-0.15	-0.27	-0.14	0.10	0.14
D4H	-0.50	-0.42	-0.11	0.09	0.18	0.17	0.27	0.42	0.04	0.50	0.42	-0.04	0.10	0.34	0.09	-0.12
D4V	-0.50	-0.19	0.01	-0.30	-0.17	-0.12	-0.01	0.50	0.18	-0.01	0.25	-0.14	0.15	0.38	-0.04	0.39

Table 4. Feature extraction value of T1WI\_2 original image

A4H	-0.50	-0.50	-0.49	-0.34	-0.20	-0.13	-0.07	0.03	0.12	0.21	0.30	0.38	0.45	0.50	0.48	0.35
A4V	-0.50	-0.49	-0.33	-0.09	-0.19	-0.12	0.04	0.12	0.23	0.39	0.34	0.39	0.50	0.44	0.50	0.50
H4V	-0.50	-0.49	-0.43	-0.33	-0.21	-0.22	-0.10	-0.13	-0.23	0.50	-0.06	0.00	-0.28	0.28	0.46	-0.14
V4H	-0.50	-0.50	-0.47	-0.41	-0.20	-0.37	-0.06	-0.20	-0.11	-0.20	0.03	0.15	-0.05	0.10	0.50	0.23
D4H	-0.50	-0.48	-0.39	-0.06	0.16	0.20	0.50	0.22	0.13	0.03	-0.04	-0.10	-0.27	-0.16	-0.24	-0.26
D4V	-0.50	-0.45	-0.05	0.00	0.21	0.45	0.50	0.36	0.27	-0.05	-0.22	0.13	0.00	-0.05	0.17	-0.07

Table 5. Feature extraction value of T1WI\_2 segmental image

A4H	-0.50	-0.50	-0.48	-0.34	-0.32	-0.30	-0.22	-0.12	-0.07	0.09	0.24	0.39	0.43	0.50	0.50	0.18
A4V	-0.50	-0.48	-0.38	-0.21	-0.33	-0.36	-0.21	-0.08	0.05	0.26	0.18	0.30	0.50	0.27	0.42	0.39
H4H	-0.50	-0.49	-0.42	-0.33	-0.23	-0.15	-0.14	0.12	0.09	0.34	0.04	0.06	-0.20	0.10	0.50	0.15
V4H	-0.50	-0.50	-0.48	-0.42	-0.19	-0.32	-0.03	0.21	0.48	0.08	0.42	-0.13	0.14	0.50	0.43	
D4H	-0.50	-0.49	-0.42	0.01	0.12	0.12	0.50	0.15	0.43	0.29	0.41	0.28	-0.25	0.08	0.08	0.23
D4V	-0.50	-0.47	-0.23	-0.18	0.04	0.21	0.49	0.50	0.28	0.13	-0.14	0.24	-0.14	0.03	0.25	-0.11

Table 6. Feature extraction value of T2WI\_1 original image

A4H	-0.50	-0.50	-0.50	-0.48	-0.33	-0.27	-0.16	0.05	0.40	0.50	0.36	0.38	0.41	0.35	0.36	0.33
A4V	-0.50	-0.50	-0.41	-0.29	-0.17	-0.03	0.04	0.09	0.16	0.08	0.05	0.16	0.40	0.50	0.41	0.36
H4V	-0.50	-0.49	-0.38	-0.32	-0.09	-0.01	0.11	0.19	0.26	0.10	0.34	0.47	0.33	0.44	0.44	0.50
V4H	-0.50	-0.50	-0.50	-0.47	-0.31	-0.18	-0.15	-0.26	-0.06	0.11	0.33	0.50	0.31	0.26	0.25	0.41
D4H	-0.50	-0.50	-0.49	-0.33	-0.20	0.17	0.21	-0.01	0.49	0.50	-0.03	-0.05	-0.18	-0.07	-0.09	0.15
D4V	-0.50	-0.41	-0.29	-0.19	-0.05	0.13	0.11	0.50	0.07	-0.17	0.04	0.42	0.31	-0.14	-0.19	-0.19

Table 7. Feature extraction value of T2WI\_1 segmental image

A4H	-0.50	-0.50	-0.50	-0.49	-0.35	-0.34	-0.22	0.09	0.50	0.38	0.22	-0.01	-0.05	-0.36	-0.14	-0.05
A4V	-0.50	-0.49	-0.44	-0.37	-0.29	-0.04	-0.12	-0.17	0.00	-0.28	-0.20	0.05	0.45	0.50	0.32	0.35
H4V	-0.50	-0.48	-0.29	-0.29	0.01	0.01	-0.14	0.11	0.26	-0.09	0.36	0.50	0.41	0.29	0.18	0.32
V4H	-0.50	-0.50	-0.50	-0.47	-0.31	-0.31	-0.31	-0.30	-0.23	-0.11	0.44	0.50	0.26	-0.13	0.00	0.08
D4H	-0.50	-0.50	-0.50	-0.35	-0.25	0.13	-0.07	-0.02	0.34	0.50	0.30	0.47	0.03	-0.09	-0.19	0.23
D4V	-0.50	-0.40	-0.35	-0.20	-0.13	-0.08	-0.11	0.50	0.05	-0.12	0.13	0.34	0.10	-0.08	-0.12	-0.16

Table 8. Feature extraction value of T2WI\_2 original image

A4H	-0.50	-0.50	-0.50	-0.46	-0.27	-0.26	-0.20	0.13	0.32	0.24	0.33	0.31	0.32	0.29	0.37	0.50
A4V	-0.50	-0.50	-0.48	-0.26	-0.02	0.21	0.24	0.21	0.23	0.30	0.31	0.29	0.50	0.47	0.38	0.45
H4V	-0.50	-0.49	-0.45	-0.41	-0.30	-0.03	0.01	0.07	0.19	-0.07	0.25	0.18	0.50	0.26	0.11	0.38
V4H	-0.50	-0.50	-0.50	-0.45	-0.37	-0.36	-0.27	0.02	0.50	0.37	0.04	0.17	0.32	0.02	0.34	0.37
D4H	-0.50	-0.48	-0.40	-0.15	-0.11	0.47	0.50	0.35	0.16	0.44	0.39	-0.01	-0.01	-0.04	0.24	0.27
D4V	-0.50	-0.45	-0.30	-0.18	0.50	0.40	-0.04	0.18	0.04	-0.18	-0.15	0.16	0.08	-0.01	0.10	0.18

Table 9. Feature extraction value of T2WI\_2 segmental image

A4H	-0.50	-0.50	-0.50	-0.44	-0.13	-0.22	-0.14	0.33	0.50	0.15	0.16	-0.04	0.02	-0.04	0.18	0.36
A4V	-0.50	-0.50	-0.44	-0.13	0.26	0.35	0.24	0.08	0.01	0.06	-0.07	-0.02	0.50	0.37	-0.06	0.08
H4V	-0.50	-0.49	-0.45	-0.36	-0.20	0.13	0.01	0.12	0.09	-0.09	0.07	0.29	0.45	0.30	0.24	0.50
V4H	-0.50	-0.50	-0.49	-0.42	-0.36	-0.37	-0.27	-0.12	0.50	0.17	0.12	0.17	0.10	-0.08	0.32	0.16
D4H	-0.50	-0.50	-0.42	-0.17	-0.21	0.13	0.09	0.39	-0.07	0.29	0.50	-0.06	-0.10	-0.07	0.00	0.07
D4V	-0.50	-0.43	-0.13	0.01	0.36	0.50	0.25	0.19	-0.20	0.00	-0.02	0.08	0.09	0.14	0.15	0.16

### 3. Training of Neural Network

Deep learning neural network models learning to map inputs to outputs given a training dataset of experiments. The training process involves finding a set of weights in the network that proves to be good, or good enough, at solving the specific problem. This training process is iterative, meaning that it progresses step by step with small updates to the model weights each iteration and, in turn, a change in the performance of the model each iteration. The iterative training process of neural networks solves an optimization problem that finds for parameters that result in a minimum error or loss when evaluating the examples in the

training dataset. In pattern recognition problems, we want a neural network to classify inputs into a set of target categories. The neural pattern recognition will help you select data, create and train a network, and evaluate its performance using cross-entropy and confusion matrices. Figure 6 shows the standard NARX(Nonlinear Autoregressive with External Input) network implemented for the experiment. The standard NARX(Nonlinear Autoregressive with External Input) network is a two-layer feedforward network with sigmoid transfer functions in the hidden layer and linear transfer functions in the output layer. The network also uses tap delay lines to store the previous values of the  $x(t)$  and

$y(t)$  sequences.  $y(t)$  As a function of  $y(t - 1)$ ,  $y(t - 2)$ , ...,  $y(t - d)$ , the output  $y(t)$  of the NARX network is fed back to the network input via delay. However, we can open this feedback loop for efficient training. Since true outputs are available during network training, the open-loop architecture above uses the actual outputs instead of feeding back the expected outputs. This has two advantages. The first is that the input to the feedforward network is more accurate. The second is that the resulting network has a pure feedforward architecture, so more efficient algorithms can be used for training. The default number of hidden neurons is set to 10. The default number of delays is two.

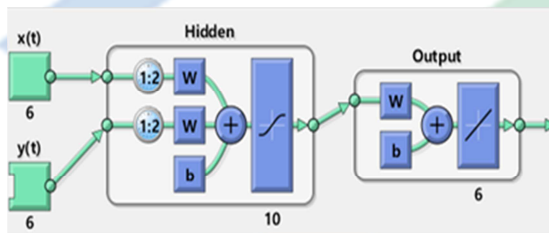


Figure 6. The neural network diagram

**(1) Result of training to T1WI**

We input the feature values extracted from two different T1-weighted original images into the neural network and trained them. The results of the training are shown in Figure 7.

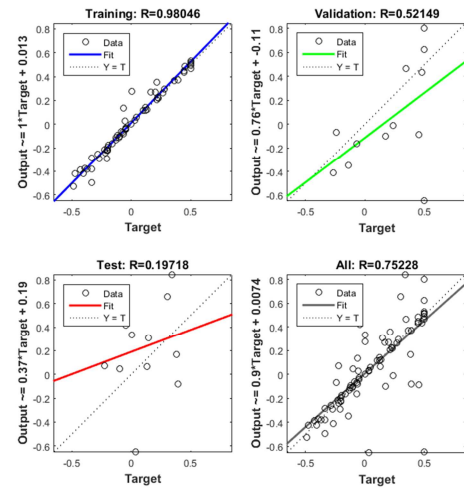


Figure 7. Regression of T1WI Original image

Figure 8 shows the results of training from the feature values extracted from two different T1 weighted segmented images into the neural network.

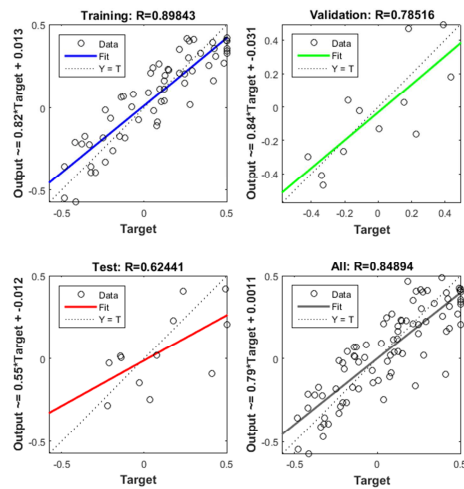


Figure 8. Regression of T1WI segmental image

**(2) Result of training to T2WI**

Figure 9 shows the results of training from the feature values extracted from two different T2 weighted original images into the neural network.

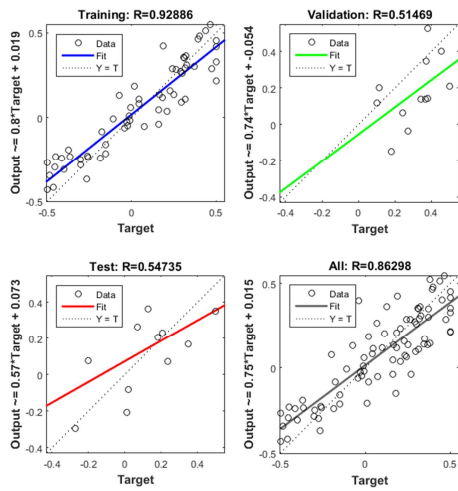


Figure 9. Regression of T2WI Original image

Figure 10 shows the results of training from the feature values extracted from two different T2 weighted segmental images into the neural network.

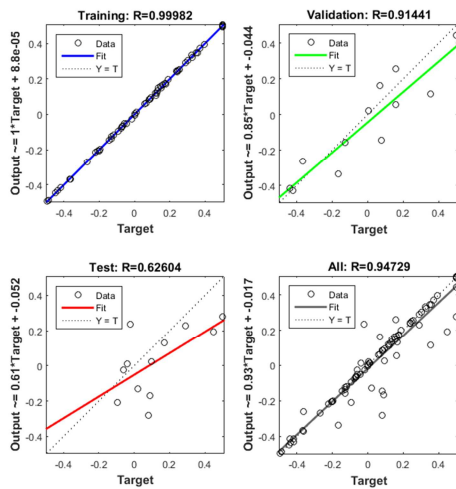


Figure 10. Regression of T2WI segmental image

**(3) Result of training to T1WI and T2WI**

Figure 11 shows the results of training from the feature values extracted from two different T1 and T2 weighted original images into the neural network.

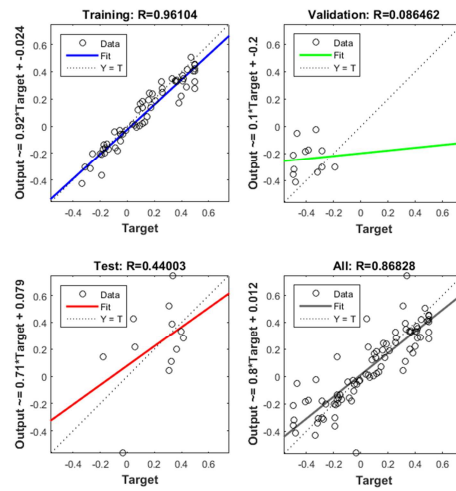


Figure 11. Regression of T1WI and T2WI Original image

Figure 12 shows the results of training from the feature values extracted from two different T1 and T2 weighted segmental images into the neural network.

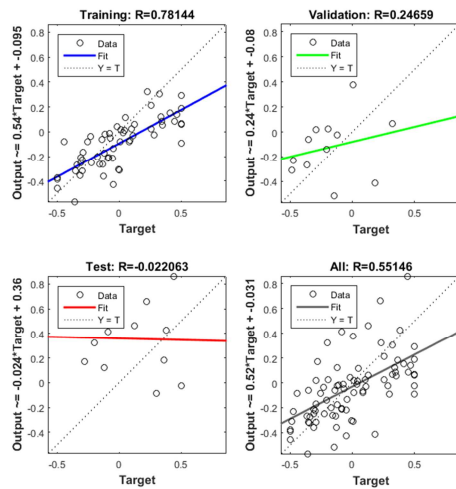


Figure 12. Regression of T1WI and T2WI segmental image

**III. Results and discussion**

To check the pattern of the extracted feature values, the graphs are shown in Figure 13 ~ 16. It can be seen that the pattern of the original

image and the segmented image are similar. The similarity of patterns suggests that segmented images typically have shape values. Therefore, if the shape value of the segmented image is used as the input value of the neural network, the learning time will be shortened and the accuracy of the learning result will be increased.<sup>[26]</sup>

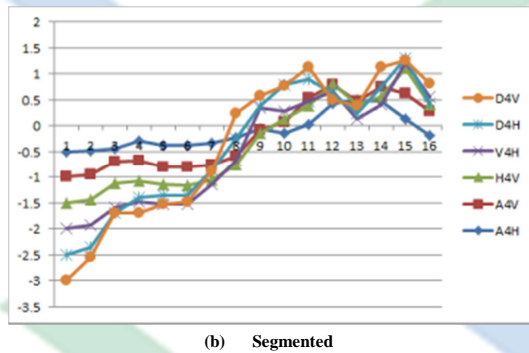
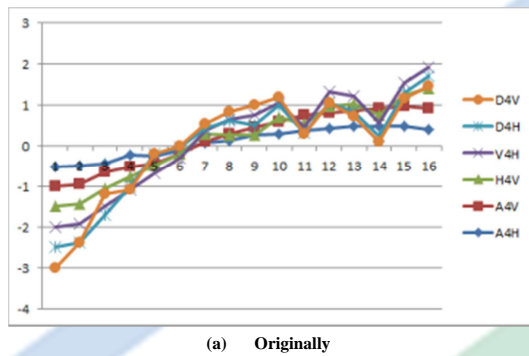


Figure 13. Feature graph of T1WI\_1 Image

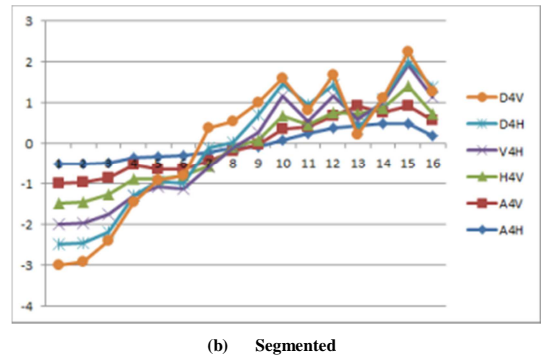
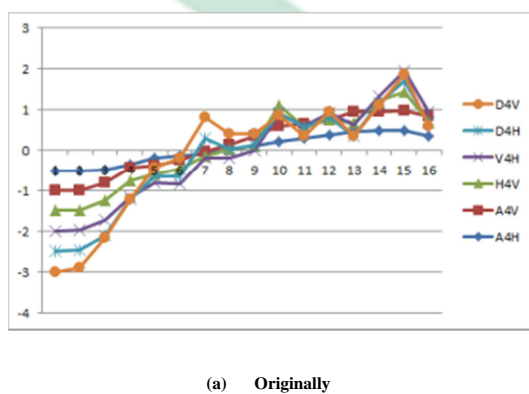


Figure 14. Feature graph of T1WI\_2 Image

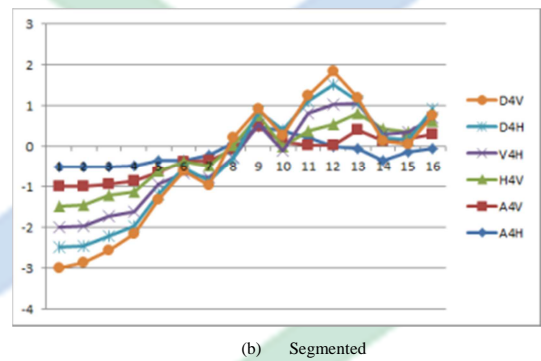
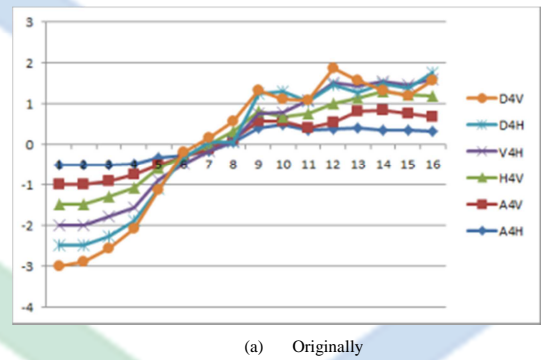
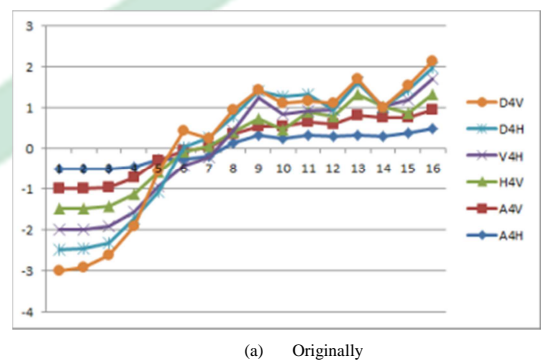
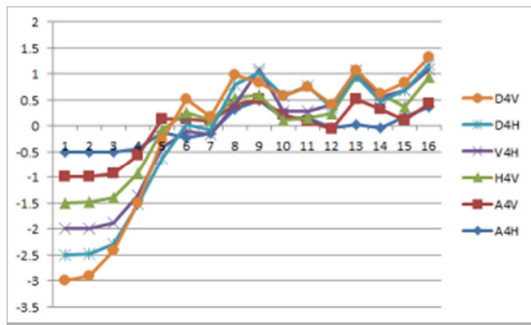


Figure 15. Feature graph of T2WI\_1 Image





(b) Segmented

Figure 16. Feature graph of T2WI\_2 Image

To evaluate the similarity between two images, the neural network was trained as follows input data : (1) Pair of T1 weighted original image, (2) Pair of T1 weighted segmental image, (3) Pair of T2 weighted original image, (4) Pair of T2 weighted segmental image, (5) T1 and T2 weighted original image, (6) T1 and T2 weighted segmental image. Figure 17 shows R values corresponding to training, validation, test, and all.

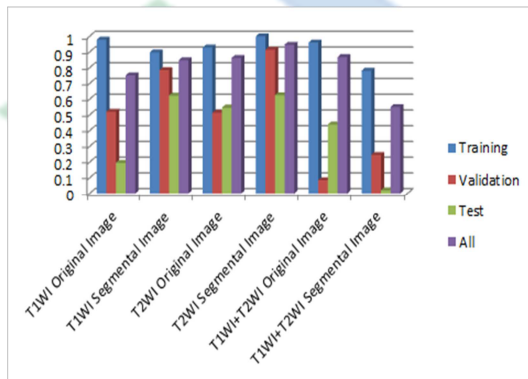


Figure 17. R-value of after running the neural network

Figure 17 shows R-values corresponding to training, validation, test, and all. In Figure 17, it can be seen that the R-value of the segmented image is closer to 1 than the original image. The reason for this is that the image obtained by segmenting the region of the weighted portion

already has similarities. Also, it can be seen that the similarity between the T1 and T2 weighted images is high in the same combination, and that the similarity is relatively low in the different weighted images. If we improve the learning result of the neural network and use the result of this study, we can classify the magnetic resonance image automatically.

#### IV. Conclusion

In this study, we proposed a method to automatically classify MRI images by neural network learning. To this end, we segmented the weighting domain of MRI. In feature extraction, the original image and segmented image were extracted by DWT, respectively. A neural network was trained by inputting extracted feature values.

As a result of the experiment, it was found that the R-value of the segmented image is closer to 1 than the original image. The reason is that the images obtained by segmenting the areas of the weighted parts already have similarities. Also, it was found that the similarity between T1 and T2 weighted images is high in the same combination, and the similarity is relatively low in different weighted images. Improving the learning results of neural networks and using this study will be able to automatically classify MR images.

Artificial intelligence must break down barriers to be widely accepted and reliable in mainstream medical imaging environments. This is because validation studies are needed to demonstrate the performance of deep learning algorithms in clinical environments.

The most important issue in medical imaging is ensuring the confidence of radiologists using artificial intelligence. To solve this problem, it is of utmost importance that the algorithm

developer and radiological technologist work together to provide a solution that is integrated with the radiologist's workflow.

#### [Reference]

- [1] Dietrich Harder, "**Röntgen's Discovery—How and Why It Happened**", International Journal of Radiation Biology and Related Studies in Physics, Chemistry and Medicine, 1987, Volume 51, issue 5, pp. 815~839.
- [2] Paulo Leitao, Armando Walter Colombo, Stamatis Karnouskos, "**Industrial automation based on cyber-physical systems technologies: Prototype implementation and challenges**", 2016, Computers in Industry, Volume 81, PP. 11~25.
- [3] Antonio dos Anjos, Hamid Reza Shahbazkia, "**Bi-Level Image Thresholding A Fast Method**", In Proceedings of the First International Conference on Bio-inspired Systems and Signal Processing, pages 70-76, DOI: 10.5220/0001064300700076.
- [4] HeikoAndra, NicolasCombaret, JackDvorkin, ErikGlatt, et al, "**Digital rock physics benchmarks-Part I: Imaging and segmentation**", 2012, Computer & Geosciences, Volume 50, PP. 25~32.
- [5] M. Lalitha, M. Kiruthiga, C. Loganathan, "**A Survey on Image Segmentation through Clustering Algorithm**", 2013, IJSR, Volume 2, Issue 2, PP. 348~358.
- [6] Koushik Mondal, Paramartha Dutta, Siddhartha Bhattacharyya, "**Fuzzy Logic Based Gray Image Extraction and Segmentation**", 2012, International Journal of Scientific & Engineering Research, Volume 3, Issue 4, PP. 1~14.
- [7] Om Prakash, Ashish Khare, "**Tracking of moving object using energy of biorthogonal wavelet transform**", 2015, Chiang Mai J. Sci, Volume 42. No. 3, pp. 783~795.
- [8] Ilkay Darilmaz, "**Wavelet Based Similarity Measurement Algorithm for Seafloor Morphology**", 2006, MIT, Master of Science in Mechanical Engineering, pp. 24~52.
- [9] Juuso Olkkonen, "**DISCRETE WAVELET TRANSFORMS – THEORY AND APPLICATION**", 2011. Books.google.com, pp181~256.
- [10] Eric J. Topol, "**High-performance medicine: the convergence of human and artificial intelligence**", 2019, nature medicine, volume 25 pp. 44~56.
- [11] Wang, X. et al. "**ChestX-ray8: hospital-scale chest X-ray database and benchmarks on weakly-supervised classification and localization of common thorax diseases.**", 2017, Preprint at <https://arxiv.org/abs/1705.02315>.
- [12] Steve G. Langer, Stephen J. Carter, David R. Haynor, et al, "**Image Acquisition: Ultrasound, Computed Tomography, and Magnetic Resonance Imaging**", 2001, World J Surg 25, pp. 1428~1437,

- doi:10.1007/s00268-001-0128-y.
- [13] Nam, J. G. et al. "**Development and validation of deep learning-based automatic detection algorithm for malignant pulmonary nodules on chest radiographs**", 2018, Radiology, <https://doi.org/10.1148/radiol.2018180237>.
- [14] Vojislav Kecman, "**Learning and Soft Computing**", 2001, The MIT Press, pp. 255~393.
- [15] Daniel S. W. Ting, Yong Liu, et al, "**AI for medical imaging goes deep**", 2018, nature medicine, volume 24, pp. 539~540.
- [16] AnantMadabhushi, GeorgeLee, "**Image analysis and machine learning in digital pathology: Challenges and opportunities**", 2016, Medical Image Analysis, Volume 33, pp. 170~175.
- [17] Ahmed Hosny, Chintan Parmar, et al. "**Artificial intelligence in radiology**", 2018, nature reviews cancer, volume 18 pp. 500~510.
- [18] Kun-Hsing Yu, Andrew L. Beam, Isaac S. Kohane, "**Artificial intelligence in healthcare**", 2018, nature biomedical engineering, volume 2, pp. 719~731.
- [19] GangWang, T.WarrenLiao, "**Automatic identification of different types of welding defects in radiographic images**", 2002, NDT & E International, Volume 35, Issue 8, pp. 519~528.
- [20] Klaus Schwab, "**The fourth industrial revolution**", 2016, books.google.com, pp. 1~25.
- [21] I L Pykett, J H Newhouse, F S Buonanno, T J Brady, et al, "**Principles of nuclear magnetic resonance imaging**", Radiology, 1982, Vol. 143, No. 1, PP. 157~168.
- [22] Satish Kumar, Raghavendra Srinivas, "**A Study on Image Segmentation and its Methods**", 2013, International Journal of Advanced Research in Computer Science and Software Engineering, Volume 3, Issue 9, pp. 1112~1114.
- [23] P. Natarajan, N Krishnan, Natasha Sandeep Kenkre, et al, "**Tumor detection using threshold operation in MRI brain images**", 2012 IEEE International Conference on Computational Intelligence and Computing Research, DOI: [10.1109/ICCIC.2012.6510299](https://doi.org/10.1109/ICCIC.2012.6510299).
- [24] Marina E. Plissiti, Christophoros Nikou, Antonia Charchanti, "**Combining shape, texture and intensity features for cell nuclei extraction in Pap smear images**", 2011, [Pattern Recognition Letters](https://doi.org/10.1007/978-1-4471-6741-9), Volume 32, Issue 6, PP. 838~853.
- [25] I. Carlbom, D. Terzopoulos, K.M. Harris, "**Computer-assisted registration, segmentation, and 3D reconstruction from images of neuronal tissue sections**", 1994, IEEE Transactions on Medical Imaging, Volume 13, Issue 2, pp. 351~362.
- [26] Zheng Liu, Hiroyuki Ukida, Pradeep Ramuhalli, Kurt Niel, "**Integrated Imaging and Vision Techniques for Industrial Inspection**", 2015, Springer, pp. 319~412, DOI : [doi.org/10.1007/978-1-4471-6741-9](https://doi.org/10.1007/978-1-4471-6741-9).

## Optimized Feature Parameter Extraction of Brain Tumor MRI

Jingyu Kim, \*SangBock Lee, Gyehwan Jin, Byungju Ahn, Jooyeon Kim, Sangjin Lim

Received: 12 October 2019 / Accepted: 21 December 2019 / Published online: 30 December 2019

©The Author(s) 2019

**Abstract-** This study aimed to extract optimized feature parameters for PET-MRI fusion imaging, a state-of-the-art medical imaging technique that has been the focus of much recent research. The medical images obtained from this technique are characterized by high resolution and low exposure dose.

A neural network was trained by inputting extracted feature values. As a result of the experiment, it was found that the R-value of the segmented image is closer to 1 than the original image. The reason is that the images obtained by segmenting the areas of the weighted parts already have similarities. Also, it was found that the similarity between T1 and T2 weighted images is high in the same combination, and the similarity is relatively low in different weighted images. The most important issue in medical imaging is ensuring the confidence of radiologists using artificial intelligence. To solve this problem, it is of utmost importance that the algorithm developer and radiological technologist work together to provide a solution that is integrated with the radiologist's workflow.

*Jingyu Kim*

*Dept. of Radiology, Nambu University, Graduate School*  
*e-mail : [jingyu8754@naver.com](mailto:jingyu8754@naver.com)*

\*SangBock Lee(✉) **corresponding author**

*Dept. of Radiology, Nambu University*  
*e-mail : [sblee@nambu.ac.kr](mailto:sblee@nambu.ac.kr)*

*Gyehwan Jin*

*Dept. of Radiology, Nambu University*  
*e-mail : [ghjin@nambu.ac.kr](mailto:ghjin@nambu.ac.kr)*

*Byungju Ahn*

*Dept. of Radiology, Nambu University*  
*e-mail : [anju6010@nambu.ac.kr](mailto:anju6010@nambu.ac.kr)*

*Jooyeon Kim*

*Korea Basic Science Institute*

*e-mail : [jooyun8992@kbsi.re.kr](mailto:jooyun8992@kbsi.re.kr)*

*Sangjin Lim*

*GAIHST, Gachon University*

*e-mail : [mailto:touphgh94@gmail.com](mailto:mailto:touphgh94@gmail.com)*

**Key word: MRI, Image Processing, Discrete Wavelet Transform, Segmentation**

### I. Introduction

Noninvasive imaging at the molecular level is an emerging field in biomedical research. PET-MRI fusion image is a new technology synergizing two leading imaging methodologies: positron emission tomography (PET) and magnetic resonance imaging (MRI). Although the value of PET lies in its high-sensitivity tracking of biomarkers in vivo, it lacks

resolving morphology. MRI has lower sensitivity, but produces high soft-tissue contrast and provides spectroscopic information and functional MRI (fMRI). PET-MRI provides a powerful tool for studying biology and pathology in preclinical research and has great potential for clinical applications. Combining fMRI and spectroscopy with PET paves the way for a new perspective in molecular imaging.[1] With the increasing use of direct digital imaging systems for medical diagnostics, digital image processing becomes more and more important in health care. In addition to originally digital methods, such as Computed Tomography (CT) or Magnetic Resonance Imaging (MRI), initially analog imaging modalities such as endoscopy or radiography are nowadays equipped with digital sensors. Digital images are composed of individual pixels, to which discrete brightness or color values are assigned. They can be efficiently processed, objectively evaluated, and made available at many places at the same time by means of appropriate communication networks and protocols, such as Picture Archiving and Communication Systems (PACS) and the Digital Imaging and Communications in Medicine (DICOM) protocol, respectively. Based on digital imaging techniques, the entire spectrum of digital image processing is now applicable in medicine.[2] Histogram equalization is widely used for medical image processing because of its simple features and effects. In this paper, we enhance the image by histogram equalization. Brain image segmentation is one of the most important parts of clinical diagnostic tools. Brain images mostly contain noise, inhomogeneity and sometimes deviation. Therefore, accurate segmentation of brain images is a very difficult task. However, the process of accurate segmentation of these images is very important and crucial for a

correct diagnosis by clinical tools[3]. Segmented the brain image by setting the appropriate threshold in images with various pixel values[4]. We propose a method of extracting optimal feature values after decomposing a segmented image by DWT. The extracted feature values may be useful for image analysis and treatment planning.

## II. Materials and methods

### 1. Medical image processing by MATLAB

MATLAB is a data analysis and visualization tool that has been designed with powerful support for matrices and matrix operations[5]. As well as this, MATLAB has excellent graphics capabilities and its own powerful programming language. One of the reasons that MATLAB has become such an important tool is through the use of sets of MATLAB programs designed to support a particular task. These sets of programs are called toolboxes, and the particular toolbox of interest to us is the image processing toolbox. In this paper, we used the image toolbox for medical image processing[5]. We shall introduce functions, commands, and techniques as required. A MATLAB function is a keyword that accepts various parameters and produces some sort of output: for example a matrix, a string, a graph or figure[5]. Examples of such functions are `sin`, `imread`, `imclose`. There are many functions in MATLAB, it is very easy to write our own. MATLAB, we can combine functions and commands, or put multiple commands on a single input line. MATLAB's standard data type is the matrix—all data are considered to be matrices of some sort. Images, of course, are matrices whose elements are the grey values of its pixels[6]. It is single values are considered by MATLAB to be  $1 \times 1$  matrices, while a string is merely a  $1 \times n$  matrix of characters.

**2. Image segmentation**

In digital image processing, image segmentation is the process of dividing a digital image into segments. The goal of segmentation is to simplify or change the representation of the image to something more meaningful and easier to analyze.[7][8] Image segmentation is commonly used to find objects and boundaries (lines, curves, etc.) in an image. More precisely, image segmentation is the process of assigning a label to every pixel in an image so that pixels with the same label share specific characteristics. The result of the image segmentation is a set of segments that collectively covered with a set of contours extracted from the whole image or the image.[9][10] Each pixel in the area is similar in terms of some characteristics or calculated properties, such as intensity. The adjacent region varies considerably concerning for the same characteristics.[11] The simplest method of image segmentation is called the threshold method. This method converts grayscale images to binary images based on the clip level. The key to this method is to choose a threshold. In this paper, we segmented the image in the following way;

$$BW = \text{imsefmm}(W, \text{mask}, \text{thresh})$$

$BW = \text{imsefmm}(W, \text{mask}, \text{thresh})$  returns a segmented image  $BW$ , which is computed using the Fast Marching Method. The array  $W$  specifies weights for each pixel.  $\text{mask}$  is a logical array that specifies seed locations.  $\text{thresh}$  is a non-negative scalar in the range  $[0 \ 1]$  that specifies the threshold level.

**3. Discrete Wavelet Transform(DWT)**

Wavelet transform was proposed in the mid-1980s, and it has been used in various fields such as signal processing, image processing, computer

vision, image compression, biochemistry medicine, etc.[12] For image processing, it provides an extremely flexible multi-resolution image and can decompose an original image into different subband images including low- and high-frequencies. Therefore people can choose the specific resolution data or subband images upon their demands.[13] A 2-D DWT of an image is illustrated in Figure 3(a). When the original image is decomposed into four-subband images, it has to deal with row and column directions separately. First, the high-pass filter  $G$  and the low-pass filter  $H$  are exploited for each row data, and then are down-sampled by 2 to get high- and low-frequency components of the row. Next, the high- and the low-pass filters are applied again for each high- and low-frequency components of the column, and then are down-sampled by 2.[14] By way of the above processing, the four-subband images are generated:  $HH$ ,  $HL$ ,  $LH$ , and  $LL$ . Each subband image has its feature, such as the low-frequency information is preserved in the  $LL$ -band and the high-frequency information is almost preserved in the  $HH$ -,  $HL$ -, and  $LH$ -bands. The  $LL$ -subband image can be further decomposed in the same way for the second level subband image.[15] By using 2-D DWT, an image can be decomposed into any level of subband images, as shown in Figure 3(b).

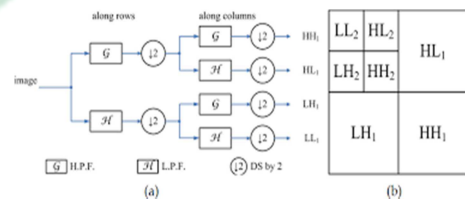


Figure 1. Diagrams of DWT image decomposition: (a) the 1-L 2-D analysis DWT image decomposition process, (b) the 2-L 2-D analysis DWT subband.[11]

#### 4. Neural Networks

Artificial intelligence (AI) has led to many medical advancements, from AI-based software for the management of medical records to diagnosing and recognizing conditions.[16] Most of the new work on artificial intelligence in the medical field is related to diagnostic technology, and AI systems are trained to recognize the characteristics of various conditions.<sup>[17][18]</sup> Through ‘machine learning’ (ML), AI provides techniques that uncover complex associations that cannot easily be reduced to an equation.<sup>[19]</sup> For example, neural networks represent data through vast numbers of interconnected neurons in a similar fashion to the human brain. This allows ML systems to approach complex problem solving just as a clinician might by carefully weighing evidence to reach reasoned conclusions.<sup>[20]</sup> However, unlike a single clinician, these systems can simultaneously observe and rapidly process an almost limitless number of inputs. Furthermore, these systems can learn from each incremental case and can be exposed, within minutes, to more cases than a clinician could see in many lifetimes. Artificial intelligence complements the vast number of digital images created in hospitals, the products of next-generation imaging scanners, especially hybrids that include MRI, CT, PET, and SPECT. In recent years, machine learning algorithms are rapidly being used in medical image analysis.[21][22] These machine learning techniques are used to extract compact information to improve the performance of medical image analysis. Recently, deep learning methods using deep convolutional neural networks have been applied to medical image analysis to provide promising results.<sup>[21][22]</sup> The neural network model is shown in Figure 2 below.

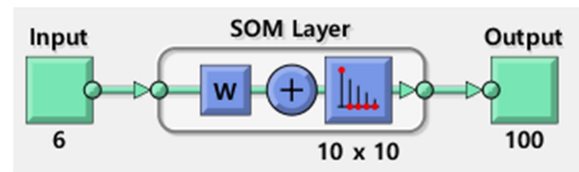


Figure 2. A neural network model

Applications cover the full spectrum of medical image analysis, including detection, segmentation, classification, and computer-assisted diagnostics.<sup>[23]</sup> As a result, if artificial intelligence and healthcare professionals interact to accommodate deep thinking platforms, such as automation, in diagnosing a patient's disease state, artificial intelligence will play an important role in the analysis of medical image data, which will only be feasible.<sup>[24][25]</sup>

#### I. Experiments and results

Digital image processing is the use of computer algorithms to perform image processing on digital images. As a subfield of digital signal processing, digital image processing has many advantages over analog image processing. It allows a much wider range of algorithms to be applied to the input data. The aim of digital image processing is to improve the image data by suppressing unwanted distortions and enhancement of some important image features so that our AI-Computer Vision models can benefit from this improved data to work on. For the experiment, we acquired brain tumor MRI from The Cancer Imaging Archive site. The image was preprocessed to 256 x 256 pixels for segmentation and stored in a bitmap format. The stored images were segmented with 127 ~ 200 as the threshold. Six parameters per image were extracted from the segmented image using DWT. We learned neural networks by inputting extracted parameters into the neural networks. Figure 5 is a flow chart showing the whole process of the experiment.

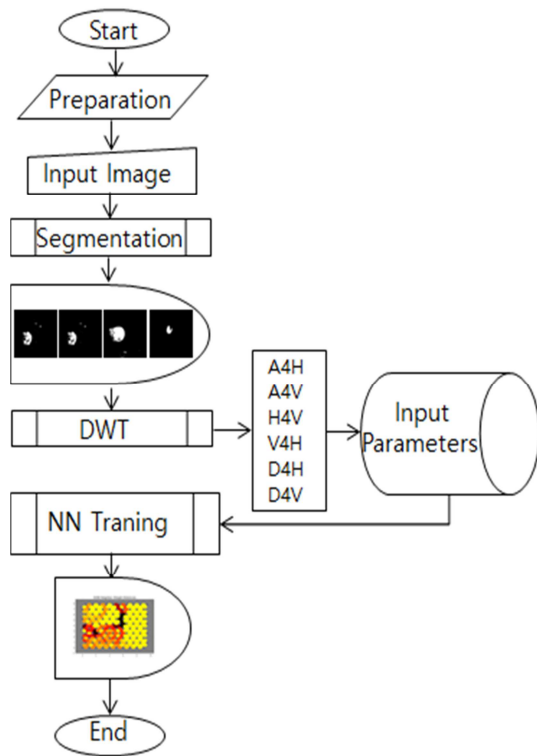


Figure 2. Experiment Flowchart

Table 1. Image segment and edge

	Original	Segment	Edge
<b>Image1</b>			
<b>Image2</b>			
<b>Image3</b>			
<b>Image4</b>			

### 1. Segmentation by MATLAB Program

In medical image segmentation, thresholding is a simple, yet effective, way of partitioning an image into a lesion and other regions. This image analysis technique is a type of image segmentation that isolates objects by converting grayscale images into binary images. In this study, we segmented four brain tumor MRI images (images 1 to 4). The segmented results are shown in Table 1.

### 2. Feature Extraction by DWT

We performed a program using MATLAB Tool Box to extract brain tumor MRI features. The six parameters for feature extraction are horizontal low frequency (A4H), vertical low frequency (A4V), horizontal high frequency (H4V), vertical high frequency (V4H), horizontal diagonal high frequency (D4H), and vertical diagonal high frequency (D4V). A total of 96 features were extracted by extracting 16 feature values for each parameter. Table 2 shows the meanings and abbreviations of the feature parameters of the coefficient matrix.

Table 2. Feature parameters of the coefficient matrix.

Abbreviation	Feature extraction parameter
A4H	Horizontal low frequency
A4V	Vertical low frequency
H4V	Horizontal high frequency
V4H	Vertical high frequency
D4H	Diagonal High frequency (horizontal)
D4V	Diagonal High frequency (vertical)

Tables 3 to 10 show the segmented parameter display and the characteristic values of the original image and the segmented image as graphs. It was confirmed that the slope change of the graph was large in the feature value of the segmented image. The reason for

this is that the part corresponding to the background part of the image is removed during the segmentation process and the part with the lesions has a high frequency.

Table 3. Feature extraction value of MRI\_Brain\_Tumor1\_Seg.pgm image

A4H	-0.5	-0.5	-0.5	-0.5	-0.5	-0.5	-0.4	-0.26	-0.4	-0.3	-0.33	0.43	0.5	-0.49	-0.45	-0.09
A4V	-0.5	-0.5	-0.5	-0.5	-0.5	-0.5	-0.5	-0.5	-0.48	-0.5	-0.5	-0.47	-0.39	-0.5	-0.46	0.5
H4V	-0.5	-0.5	-0.5	-0.5	-0.5	-0.5	-0.5	-0.48	-0.39	-0.5	-0.48	-0.45	-0.31	-0.5	-0.42	0.5
V4H	-0.5	-0.5	-0.5	-0.5	-0.5	-0.5	-0.47	-0.46	-0.39	-0.3	-0.39	0.12	0.5	-0.49	-0.49	-0.4
D4H	-0.5	-0.5	-0.5	-0.5	-0.5	-0.4	-0.24	-0.37	0.5	-0.3	-0.04	-0.03	0.37	-0.49	-0.35	-0.18
D4V	-0.5	-0.5	-0.5	-0.5	-0.5	-0.5	-0.5	-0.47	-0.49	-0.5	-0.5	-0.43	-0.48	-0.5	-0.37	0.5

Table 4. Feature Extraction in brain MRI tumor1 image.

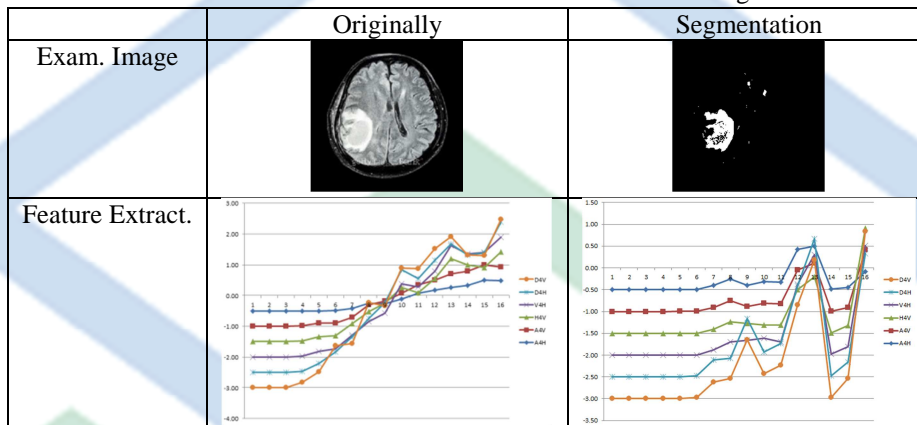


Table 5. Feature extraction value of MRI\_Brain\_Tumor2\_Seg.pgm image

A4H	-0.5	-0.5	-0.5	-0.5	-0.50	-0.4	-0.2	-0.05	-0.02	0.27	0.43	0.48	0.50	0.50	0.48	0.3
A4V	-0.5	-0.5	-0.5	-0.5	-0.50	-0.5	-0.5	-0.50	-0.50	-0.50	-0.50	-0.50	-0.47	0.08	0.48	0.5
H4V	-0.5	-0.5	-0.5	-0.5	-0.50	-0.5	-0.5	-0.50	-0.50	-0.50	-0.50	-0.49	-0.42	-0.09	-0.09	0.5
V4H	-0.5	-0.5	-0.5	-0.5	-0.49	-0.4	0.01	0.11	-0.01	0.50	-0.16	-0.26	-0.16	-0.15	-0.39	0.3
D4H	-0.5	-0.5	-0.5	-0.5	-0.44	0.3	0.5	0.23	0.16	0.20	-0.39	-0.40	-0.49	-0.44	0.14	0.3
D4V	-0.5	-0.5	-0.5	-0.5	-0.50	-0.5	-0.5	-0.50	-0.50	-0.50	-0.50	-0.48	-0.06	0.50	-0.36	-0.3

Table 6. Feature Extraction in brain MRI tumor2 image.

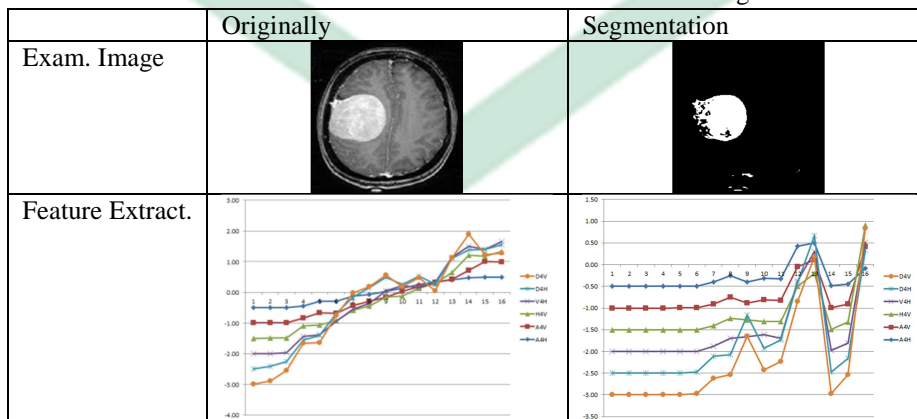


Table 7. Feature extraction value of MRI\_Brain\_Tumor3\_Seg.pgm image

A4H	-0.5	-0.5	-0.5	-0.5	-0.5	-0.5	-0.5	-0.5	-0.5	-0.5	-0.5	-0.5	-0.5	-0.45	-0.04	0.5	0.5
A4V	-0.5	-0.5	-0.5	-0.5	-0.5	-0.5	-0.5	-0.5	-0.5	-0.5	-0.5	-0.5	-0.46	-0.12	0.21	0.5	0.5
H4V	-0.5	-0.5	-0.5	-0.5	-0.5	-0.5	-0.5	-0.5	-0.5	-0.5	-0.5	-0.49	-0.47	-0.09	0.5	0.3	-0.05
V4H	-0.5	-0.5	-0.5	-0.5	-0.5	-0.5	-0.5	-0.5	-0.5	-0.5	-0.5	-0.5	-0.5	-0.48	-0.36	0.27	0.5
D4H	-0.5	-0.5	-0.5	-0.5	-0.5	-0.5	-0.5	-0.5	-0.5	-0.5	-0.5	-0.5	-0.5	-0.42	0.5	0.15	0.01
D4V	-0.5	-0.5	-0.5	-0.5	-0.5	-0.5	-0.5	-0.5	-0.5	-0.5	-0.5	-0.43	-0.05	0.47	0.33	0.5	0.11

Table 8. Feature Extraction in brain MRI tumor3 image.

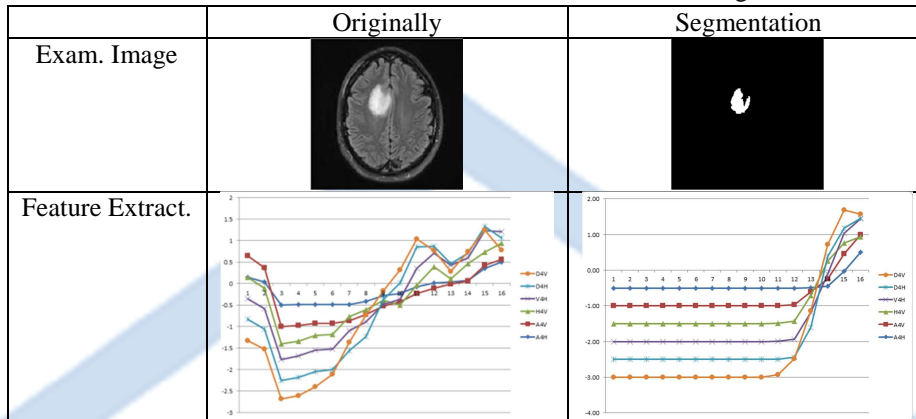
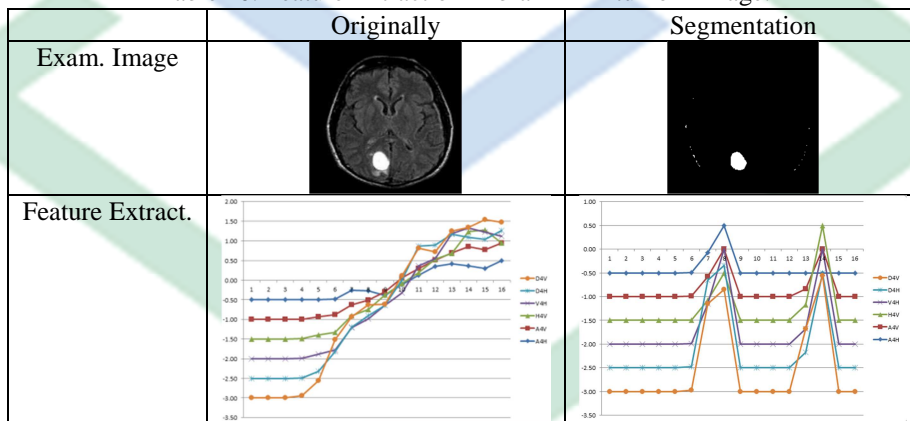


Table 9. Feature extraction value of MRI\_Brain\_Tumor4\_Seg.pgm image

A4H	-0.5	-0.5	-0.5	-0.5	-0.5	-0.49	-0.08	0.5	-0.5	-0.5	-0.5	-0.5	-0.5	-0.34	0.5	-0.5	-0.5
A4V	-0.5	-0.5	-0.5	-0.5	-0.5	-0.5	-0.5	-0.5	-0.5	-0.5	-0.5	-0.5	-0.5	-0.34	0.5	-0.5	-0.5
H4V	-0.5	-0.5	-0.5	-0.5	-0.5	-0.49	-0.08	0.5	-0.5	-0.5	-0.5	-0.5	-0.5	-0.5	-0.5	-0.5	-0.5
D4H	-0.5	-0.5	-0.5	-0.5	-0.5	-0.49	0.5	-0.35	-0.5	-0.5	-0.5	-0.5	-0.5	-0.5	-0.5	-0.5	-0.5
D4V	-0.5	-0.5	-0.5	-0.5	-0.5	-0.5	-0.5	-0.5	-0.5	-0.5	-0.5	-0.5	-0.5	0.5	-0.06	-0.5	-0.5

Table 10. Feature Extraction in brain MRI tumor4 image.



### 3. Self-organizing map using NN

A self-organizing map (SOM) consists of a competitive layer that can classify a dataset of vectors with any number of dimensions into as many classes as the layer has neurons. The neurons are arranged in a 2D topology, which allows the layer to form a representation of the distribution and a two-dimensional approximation of the topology of the

dataset. Self-organizing maps learn to cluster data based on similarity, topology, with a preference of assigning the same number of instances to each class. Self-organizing maps are used both to cluster data and to reduce the dimensionality of data. Tables 11 to 14 show original and segmented images of self-organizing maps of four brain tumor MRIs,

respectively. The self-organizing maps in each table represent Neighbor Weight Distances, Neural Networks Training self-organizing map Input Planes, and Neural Networks Training self-organizing map Sample Hits.

and Neural Networks Training self-organizing map Sample Hits.

Table 11. Self-organizing map of brain MRI tumor1 image

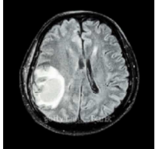
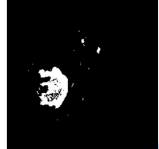
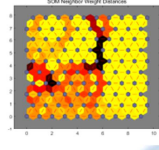
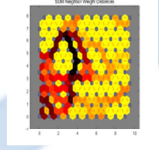
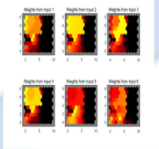
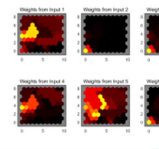
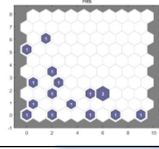
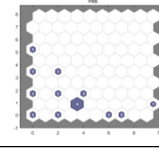
	Originally	Segmentation
Exam. Image		
SOM Neighbor Weight Distances		
NN Training SOM Input Planes		
NN Training SOM Sample Hits		

Table 13. Self-organizing map of brain MRI tumor3 image

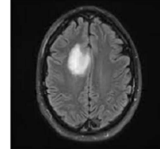
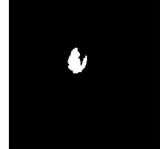
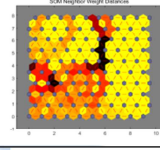
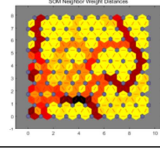
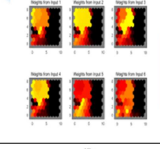
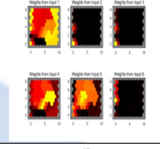
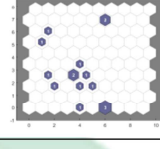
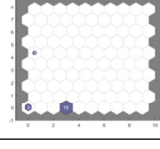
	Originally	Segmentation
Exam. Image		
SOM Neighbor Weight Distances		
NN Training SOM Input Planes		
NN Training SOM Sample Hits		

Table 12. Self-organizing map of brain MRI tumor2 image

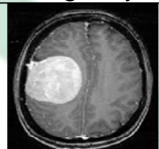
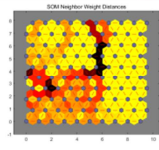
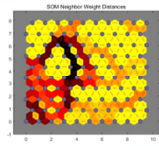
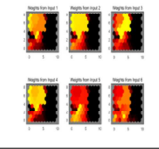
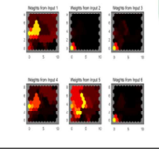
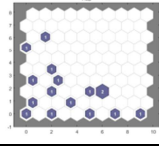
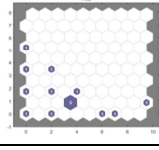
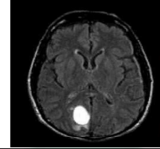
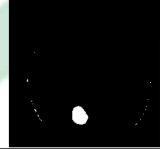
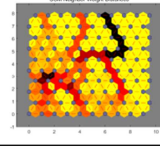
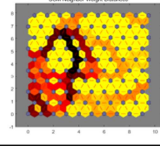
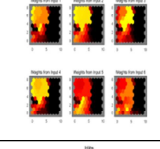
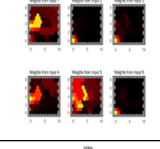
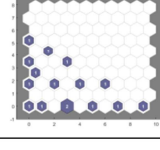
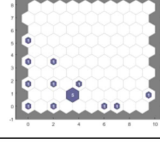
	Originally	Segmentation
Exam. Image		
SOM Neighbor Weight Distances		
NN Training SOM Input Planes		
NN Training SOM Sample Hits		

Table 14. Self-organizing map of brain MRI tumor4 image

	Originally	Segmentation
Exam. Image		
SOM Neighbor Weight Distances		
NN Training SOM Input Planes		
NN Training SOM Sample Hits		

#### IV. Conclusion

In this study, we proposed a method of segmenting tumor lesions and extracting optimal feature parameters from brain tumor MRI. To this end, brain tumor images were segmented and edge was detected at the segment. The detected edge becomes the exact region of interest of the brain tumor lesion. The segmentation image was decomposed by DWT and 96 features were extracted with 6 variables. To evaluate the extracted feature values, we compared the extracted feature values with the values of the original image. As a result of the comparison, the patterns of change were similar, and the extracted feature values were found to be largely changed at a specific portion. Also, the neural network identified the self-organizing map(SOM) Neighbor Weight Distances, Neural Networks Training self-organizing map(SOM) Input Planes, and Neural Networks Training self-organizing map(SOM) Sample Hits. As a result, the deviation of the pixel neighbor values in the segmented image was large. Perhaps, the reason is that it contains feature values. If the feature extraction method proposed in this study is used, it will be able to be used for disease recognition by AI and automatic diagnosis of medical images.

#### Conflict of Interest

The author(s) declare(s) that there is no conflict of interest regarding the publication of this article.

#### Acknowledgments

This study was supported by Nambu University research fund of 2017.

#### [Reference]

- [1] Martin S Judenhofer, Hans Wehrl, Ciprian Catana, “*Simultaneous PET-MRI: a new approach for functional and morphological imaging*”, 2008, Nature medicine, Vol. 14, No. 4, pp. 459~465.
- [2] T. M. Deserno, “*Biomedical Image Processing*”, 2011, Springer, pp. 4~51, DOI:10.1007/978-3-642-15816-2\_1
- [3] Mohammad Ali Balafar, Abdul Rahman Ramli, M Iqbal Saripan, Syamsiah Mashohor, “*Review of brain MRI image segmentation methods*”, 2010, Artificial Intelligence Review, Vol. 33. No. 3, pp. 261~274.
- [4] G.E. Sujji, Y.V.s. Lakshmi, Wiselin Jiji, “*MRI Brain Image Segmentation based on Thresholding*”, 2013, International Journal of Advanced Computer Research, Vol. 3, No. 1, pp. 97~101
- [5] <https://kr.mathworks.com/help/matlab/>
- [6] Alasdair McAndrew, “*An Introduction to Digital Image Processing with Matlab*”, School of Computer Science and Mathematics, Victoria University of Technology, pp. 33~128.
- [7] Rajvardhan Oak, “*A Study of Digital Image Segmentation Techniques*”, 2016, International Journal Of Engineering And Computer Science, Vol. 5, Issue 12, pp. 19779~19783.
- [8] <https://www.analyticsvidhya.com/blog/2019/04/introduction-image-segmentation-techniques-python/>
- [9] Krishna Kant Singh, Akansha Singh, “*A Study of Image Segmentation Algorithms for Different Type of Images*”, 2010, IJCI, Vol. 7, Issue 5, pp. 1694~1698.
- [10] Varshali Jaiswal, Aruna Tiwari, “*A Survey of Image Segmentation based on Artificial Intelligence and Evolutionary Approach*”, 2013, IOSR-JCE, vol. 15, Issue 3, pp. 71~78.
- [11] <https://courses.cs.washington.edu/courses/cse576/book/ch10.pdf>
- [12] Om Prakash, Ashish Kare, “*Wavelet Based Similarity Measurement Algorithm for Seafloor Morphology*”, 2006, MIT, Master of Science in Mechanical Engineering, pp. 24~52.
- [13] Juuso Olkkonen, “*Discrete Wavelet Transforms – Theory and Application*”, 2011, Books.google, pp. 181~256.
- [14] Ping-Sing Tsai, Tinku Acharya, “*Image Up-Sampling Using Discrete Wavelet Transform*”, 2006, 9th Joint International Conference on Information Sciences (JCIS-06), DOI:10.2991/jcis.2006.340
- [15] Hannu Olkkonen, “*Discrete Wavelet Transforms: Biomedical Applications*”, 2011, ISBN : 9533076542, pp.135~221.
- [16] Eric J. Topol, “*High-performance medicine: the convergence of human and artificial intelligence*”, 2019, nature medicine, Vol. 25, No. 1, pp.44~56.

- [17] AN Ramesh, C Kambhampati, et al, “**Artificial intelligence in medicine**”, 2004, Ann R Coll Surg Engl., Vol. 86, No. 5, PP.334~338.
- [18] Ahmed Hosny, Chintan Parmar, John Quackenbush, Lawrence H. et al, “**Artificial intelligence in radiology**”, 2018, nature review cancer, Vol. 18, pp. 500~510.
- [19] Varun H Buch, Irfan Ahmed and Mahiben Maruthappu, “**Artificial intelligence in medicine: current trends and future possibilities**”, 2018, British Journal of General Practice, 68(668), DOI: 10.3399/bjgp18X695213
- [20] Grégoire Montavon, Wojciech Samek, Klaus-Robert Müller, “**Methods for interpreting and understanding deep neural network**”, 2018, Digital Signal Processing, Vol. 73, pp. 1~15
- [21] A Qayyum, SM Anwar, M Majid, et al, “**Medical Image Analysis using Convolutional Neural Networks: A Review**”, 2018, Journal of Medical Systems, vol. 42, Article No: 226
- [22] Saddam Hussain ; Syed Muhammad Anwar ; Muhammad Majid, “**Brain tumor segmentation using cascaded deep convolutional neural network**”, 2017, 2017 39th Annual International Conference of the IEEE Engineering in Medicine and Biology Society (EMBC), INSPEC Accession Number: 17189504
- [23] Stefan Bauer, Roland Wiest, Lutz-P Nolte, Mauricio Reyes “**A survey of MRI-based medical image analysis for brain tumor studies**”, 2013, Physics in Medicine & Biology, Vol. 58, No. 13, pp. 1~44.
- [24] Bauer S, Wiest R, Nolte LP, Reyes M., “**A survey of MRI-based medical image analysis for brain tumor studies**”, 2013, Phys Med Biol, Vol. 58, No. 13, pp. R97~129
- [25] Filippo Pesapane, Caterina Volonte, Marina Codari, Francesco Sardanelli, “**Artificial intelligence as a medical device in radiology: ethical and regulatory issues in Europe and the United States**”, 2018, Insights into Imaging, Vol. 9, pp. 745~753.

## Ethics in Publication

Article reprints from ScholarGen Publishers commit to promote your research work with its professional quality reprints service delivered directly to your door at an affordable value. It aims to display the potential of the article at interviews, conferences, distribution to colleagues, seminars and other promotional activities. Reprints are produced from the final PDF of the article.

As all articles are open access, readers are free to download and/or print copies from the website, according to the terms & conditions of the ScholarGen Publishers License . Authors must agree to distribute such reprints without any alterations, additions, deletions, overprinting, highlighting, promotional messages, or promotional attachments.

**Author Reprints :** Author reprints are solely for the author's personal, noncommercial use. Author reprints are available in both B/W and color format with the addition of a standard cover page. Each article reprint is available with cover pages of the journal itself in order to maximum the impact and highlight the prestige of the content.

The front cover of the Reprints consists of :

- Publisher logo
- Name/logo of the journal
- Title of article, complete list of authors, and Article information

**Commercial Reprints :** Commercial reprints are high quality with specially designed covers. The reprints are an exact replica of the published article. These reprints are available only in the color format with the customized cover page.

**Ethical Principles:** Authors are expected to stick to the ethical standards and conduct that remain mandatory in scholarly publishing. During the submission, authors need to mention that their work has not been submitted elsewhere, instances (if any) & conflicts need to be stated and plagiarism must be strictly cross checked. For Animal/ Human models, ethical authorization copy needs to be submitted.

**Breach of copyright/ Plagiarism:** Plagiarism can be defined as making a replica of the published content. ScholarGen Publishers strictly against the Plagiarism. We cross check every submission that is been submitted to any of its peer reviewed Journal. Any submission that has partially /completely plagiarized content will be rejected immediately after submission.

**Attribution Practice:** Citations need to be acknowledged for previously published content. It is obligatory when new ideas or results are produced. If the author fails to reproduce citation for any previous work, it will be considered as technical plagiarism and the paper might be rejected immediately.

**Conflicts of Interest:** ScholarGen Publishers involves double blind peer review system to avoid conflicts for the submitted manuscript. The authors should hold responsibility in providing conflicts if any to avoid further conflicts.

**Confidentiality Protection:** Editors, Reviewers need to be very cautious while handling the research work of the authors. It is ethically not accepted to use/disseminate the unpublished work. Use of the unpublished work might consider for legal actions.

**Human and Animal Rights:** Clear statements of ethical clearance documents need to be provided if applicable. The work involving animal models and human volunteers need to submit the essential statements.

**Consents/Instances:** Author needs to state consents and instances if any to avoid further obligations. Clear statement with written signature must be presented by the author while submitting his/her work.

**Civility & Misconduct Allegations:** Editors, Reviewers, Authors & the Journal staff are expected to adhere to the basic professional courtesy. Any verbal abuse, debates and insult is highly offended by the ScholarGen Publishers. The supposed misconducts are severely offended further.

# **Scholargen Journal of Medical Imaging**

**Volume 2 Number 01 September 2019**

**Copy right Scholargen Journal of Medical Imaging, All right reserved.**

**This is identical to the Creative Commons Attribution Non-Commercial Licence.**

**Published on December 28, 2019**

**Subscription info : [office@scholargen.com](mailto:office@scholargen.com)**

**Open access on <https://scholargen.com/journals/journal-of-medical-imaging/>**